2011

The use of potential vorticity inversion to evaluate the effect of precipitation on downstream mesoscale processes

Martin Baxter
Central Michigan University, baxte1ma@cmich.edu

Phillip Schumacher
NOAA/NWSWFO Sioux Falls

Joshua Boustead
NOAA/NWSWFO Omaha

RMetS
Royal Meteorological Society

The use of potential vorticity inversion to evaluate the effect of precipitation on downstream mesoscale processes

Martin A. Baxter,[a]* Philip N. Schumacher[b]† and Joshua M. Boustead[c]†

[a]*Department of Geology and Meteorology, Central Michigan University, Mt. Pleasant, Michigan, USA*
[b]*NOAA/NWS WFO Sioux Falls, South Dakota, USA*
[c]*NOAA/NWS WFO Omaha/Valley, Nebraska, USA*

*Correspondence to: Martin A. Baxter, Central Michigan University, Dept. of Geology and Meteorology, 314 Brooks Hall, Mt. Pleasant, Michigan 48859, United States. E-mail: baxte1ma@cmich.edu

†The contributions of P. N. Schumacher and J. M. Boustead to this article were prepared as part of their official duties as US Federal Government employees.

The influence of precipitation near the surface warm front on precipitation downstream is evaluated. A two-way nested simulation is computed for two selected cases: 13–15 February 2003 and 3–5 January 2005. The results of the simulation are compared with output from the North American Regional Reanalysis dataset, which is used as a high-resolution proxy for true atmospheric conditions. The relevant physical processes in the generation and maintenance of precipitation poleward of other precipitation areas are analysed, along with perturbation potential vorticity (PV) fields. Piecewise PV inversion is used to determine height and wind fields associated with the perturbation PV. These height and flow fields are used to compute derived quantities such as balanced deformation, balanced temperature perturbation, and balanced moisture flux. Both cases illustrate that the role of rainfall near surface warm fronts on precipitation downstream is complex, and is associated with more than just moisture flux. The strength, depth and orientation of diabatically generated PV anomalies within these areas of rainfall are associated with mesoscale processes relevant to the maintenance of downstream precipitation. Lastly, this work presents a methodology for analysing the role of precipitation in individual events. Copyright © 2011 Royal Meteorological Society

Key Words: cold season precipitation; midlatitude cyclones; diabatic effects; frontogenesis

Received 26 March 2010; Revised 14 September 2010; Accepted 19 October 2010; Published online in Wiley Online Library 12 January 2011

Citation: Baxter MA, Schumacher PN, Boustead JM. 2011. The use of potential vorticity inversion to evaluate the effect of precipitation on downstream mesoscale processes. *Q. J. R. Meteorol. Soc.* **137**: 179–198. DOI:10.1002/qj.730

1. Introduction

The impact of upstream rainfall upon winter storm precipitation distribution has been a question for forecasters. Many area forecast discussions (AFDs) issued by the United States (US) National Weather Service (NWS) contain reference to the potential for precipitation across the southern USA to 'rob' or inhibit the flow of moisture downstream (examples can be found in Mahoney and Lackmann, 2007). This preconception has been used as a reason to lower quantitative precipitation forecasts downstream because of expected or ongoing precipitation. Forecasters have experienced events where precipitation may be diminished and events where the precipitation does not appear to be reduced. Overall, there is a lack of understanding of the role of precipitation that occurs in close proximity to, but downstream from, a second area of precipitation.

The manner in which moisture, lift and instability organize to create frozen precipitation in either banded

or non-banded form has been previously investigated by Nicosia and Grumm (1999), Banacos (2003), Jurewicz and Evans (2004), Novak *et al.* (2004) and Moore *et al.* (2005), among others. This research demonstrates that the mesoscale processes (frontogenesis, conditional and symmetric instability) attendant with frozen precipitation can be viewed as the result of interactions between large-scale conveyor belts. As Schumacher (2003) notes, an understanding of synoptic-scale and mesoscale dynamics and the interactions of processes on these scales is critical to accurately diagnosing the location of precipitation bands. The lack of a 'typical' structure in both the large-scale and mesoscale fields creates the need for a process-oriented approach to analysing wintertime precipitation events.

The use of potential vorticity (PV) as a framework for atmospheric analysis was presented by Kleinschmidt (1957), and revived by Hoskins *et al.* (1985). Cyclonic PV anomalies develop below the level of maximum latent heating (Raymond and Jiang, 1990). As documented in Hoskins *et al.* (1985), Hertenstein and Schubert (1991), Fritsch *et al.* (1994), Ritchie and Holland (1997), and Rogers and Fritsch (2001), there is a large amount of variability in the efficiency with which PV will be generated diabatically, corresponding to the magnitude and type (stratiform or convective) of diabatic heating, the vertical and horizontal distribution of the heating, the persistence of the heating, the amount of ambient absolute vorticity, and the environment in which the heating takes place. PV anomalies associated with diabatic heating have been shown to have an important impact upon cyclogenesis (Davis and Emanuel, 1991; Stoelinga, 1996; Posselt and Martin, 2004; Moore *et al.*, 2008), and an influence on the distribution of precipitation associated with a midlatitude cyclone. Lackmann (2002) used a quasi-geostrophic PV inversion to show that a diabatically produced PV anomaly was associated with an enhanced low-level jet ahead of the cold front. Similarly, Brennan and Lackmann (2005) showed that the cyclonic PV anomaly associated with unforecast convection with the 25 January 2000 snowstorm along the US East Coast resulted in an underforecast of the low-level onshore flow and a stronger surface cyclone. Finally, Mahoney and Lackmann (2007) examined the speed of movement of convection over the southeast USA and its impact on downstream precipitation. They found that in cases where the squall line moved slowly to the east, the precipitation downstream was enhanced, and where the squall line accelerated ahead of the cold front, precipitation downstream was decreased.

In the events investigated by Lackmann (2002), Brennan and Lackmann (2005), and Mahoney and Lackmann (2007), the precipitation had a notable impact on the moisture flux within the warm conveyor belt through affecting the strength and orientation of the low-level jet. The magnitude of the low-level jet subsequently impacts the intensity of downstream precipitation through its influence on the amount of low-level moisture flux and convergence. The events investigated in the three aforementioned studies were all associated with cold fronts in which the precipitation was nearly parallel to the low-level jet, and the low-level jet did not go through the band of precipitation. Additionally, Novak *et al.* (2009) document three northeast USA cyclones in which frontogenesis is enhanced by diabatic heating within the snow band itself, followed by frontolysis and band dissipation, as an area of precipitation and associated diabatic heating east of the band develops. This work demonstrates that diabatic processes influence not only moisture flux, but also frontogenetical forcing. Precipitation near the warm front, where the major axis of the precipitation can be perpendicular to the low-level jet, is commonly observed with developing cold-season cyclones in the central USA. Thus, two cases that feature warm-frontal precipitation will be investigated here in order to analyse the following questions:

(1) Does the warm-frontal precipitation impact the location of the mid-level front and other mechanisms for lift?
(2) What impact does warm-frontal precipitation have on moisture transport toward downstream precipitation?
(3) What is the impact of a poor simulation of precipitation by the model on subsequent precipitation farther downstream?

In answering these questions, this article will present a methodology for analysing the role of precipitation in systems which also feature downstream precipitation.

Section 2 is an overview of the data and methods used. Sections 3 and 4 present the 13–15 February 2003 and 3–5 January 2005 cases, respectively. For each case, an event overview and an analysis of PV anomalies and their impacts on the model solution are presented. Section 5 summarizes the case-studies and provides discussion, and section 6 concludes the work.

2. Data and methods

2.1. Mesoscale model and data

In order to create a high-resolution dataset for analysis, events were simulated using Version 2.2 of the Weather Research and Forecasting – Advanced Research model (hereafter WRF), developed at the National Center for Atmospheric Research (Skamarock *et al.*, 2008). Simulations for 48 h were performed, with two-way nesting of three domains of 36, 12 and 4 km grid spacing (Figure 1(a)). Feedback between nests takes place as the mean of the nine fine grid points contained within each coarse grid cell is provided as the new value for the coarse grid point (see Skamarock *et al.* (2008) for more information). The 4 km grid encompasses the entire location where analysis will be performed using the 36 km data. The grid in the vertical comprises 50 levels, with a model top of 100 hPa (Figure 1(b)). The WRF uses a terrain-following hydrostatic pressure vertical coordinate, thus the effective vertical resolution of the model varies according to terrain height. Initial and lateral boundary conditions (updated every 3 h) came from the North American Regional Reanalysis (hereafter NARR), which has a grid spacing of 32 km and 45 vertical layers to 100 hPa (Mesinger *et al.*, 2006). The Kain–Fritsch convective parametrization was used on the two outermost domains (Kain, 2004), with explicit convection on the innermost domain. A grid spacing of 4 km has been observed to sufficiently reproduce much of the structure and evolution of squall-line convective systems depicted in 1 km simulations (Weisman *et al.*, 1997), thus 4 km is accepted as a reasonable grid spacing for representing the precipitation features in the cases examined here. Other physical parametrizations chosen include the Lin *et al.*microphysics scheme (Chen and Sun, 2002), the

Yonsei University planetary boundary layer scheme (Hong *et al.*, 2006), and the Dudhia short-wave (Dudhia, 1989) and rapid radiative transfer model long-wave (Mlawer *et al.*, 1997) radiation schemes.

The February 2003 case was initialised at 1800 UTC 13 February 2003 (from here on, dates and times will be noted in the form of DD/HH UTC, e.g. 13/18 UTC), and the January 2005 case was initialised at 0900 UTC 4 January 2005 (04/09 UTC), with the periods of interest occurring 18–24 h and 18–27 h into the simulations, respectively. Throughout the article, the NARR data will be used as a high-resolution, high-frequency proxy for the observations (Mesinger *et al.*, 2006), as upper-air observations lack the necessary spatial and temporal resolution necessary for this investigation. The NARR data were generated from 1979 onward using the three-dimensional variational data assimilation system used by the operational Eta model as it existed in April 2003. The NARR data were carefully compared with upper-air data for both cases, and no large-scale errors were observed. The precipitation generated by the NARR is similar to that observed (as discussed in detail later in this section), lending credence to the fact that the NARR data used in both cases is realistically depicting processes smaller in scale than can be resolved by the upper-air network. Fields from the WRF (36 km grid spacing) and NARR (32 km grid spacing) are compared. As will be shown, the evolution of physical processes in the WRF is considerably different from that depicted by the NARR fields, therefore rendering the small difference in grid spacing (32 vs. 36 km) used to depict the fields of secondary importance. There are no instances in which the other WRF grids (12 km and 4 km spacing) are compared with the NARR grid.

Cases were selected based on two of the authors' experience with poor forecasts from the operational NAM (North American Model) in real time during these events, where operational forecasters were unable to improve upon the numerical weather prediction (NWP) guidance provided. The retrospective WRF simulations are qualitatively similar to those of the operational NAM. In the 13–15 February 2003 case, the WRF did not simulate snowfall that *did* occur. In the 3–5 January 2005 case, the WRF simulated snowfall that *did not* occur, in roughly the same region. In both cases, the WRF simulated precipitation that *was* observed south of the area of snowfall. The differences between the WRF and the NARR facilitate understanding of the processes responsible for the precipitation discrepancies in the simulated atmosphere. This approach also highlights the extent to which numerical weather prediction models can be in error in such scenarios.

Precipitation simulated by the WRF will be compared with the analysis of precipitation from the NARR. West *et al.* (2007) noted that the NARR precipitation analyses can be associated with spurious grid scale precipitation, which occurs when convection is aliased to the smallest resolved scale of the model due to failures in the convective parametrization scheme to remove instability (Molinari and Dudek, 1992). As both events occur after 2002, the NARR analyses were generated in near-real time, with the use of radar-dominated precipitation analyses (US National Centers for Environmental Prediction stage-IV analysis) to disaggregate the daily gauge-based precipitation analyses into hourly bins (West *et al.*, 2007). As documented in Shafran *et al.* (2004), on a typical day, the gauge-based dataset consists of 8000 NWS Cooperative Network stations, 7000 NWS River Forecast Center stations, and 2500 Hourly Precipitation stations (Automated Surface Observing System (ASOS) data, and other sources, see Higgins *et al.* (2000)). Due to the fact that human-recorded observations (non-ASOS) and radar-dominated analyses are included in the NARR analysis, it is expected that inaccuracies in the measurement of frozen precipitation will be diminished. In both cases the NARR precipitation is found to be comparable to an analysis created using NWS Cooperative Network data, which has been successfully used in other studies involving frozen precipitation (e.g. Baxter *et al.*, 2005; Brennan and Lackmann, 2005). This comparison suggests that the NARR precipitation in these events was not a result of spurious grid scale precipitation. In the interest of caution, composite reflectivity from Level III post-processed NWS radar data encompassing 16 elevation scans and interpolated to the same 4 km grid as the WRF model are examined for each case in supplement to the NARR precipitation analyses.

In both cases, the amount of precipitation south of the areas of snowfall and the magnitude of the diabatically generated PV are incorrect in the WRF. Explaining why the WRF produces these values of precipitation and PV using this particular configuration for these two cases is beyond the scope of this article. It is well established that the development of convection (or lack thereof) has a nonlinear impact on the evolution of a simulation from that point onward (Zhang *et al.*, 2003, 2007), and the forecasting of convection remains challenging for current operational models (Fowle and Roebber, 2003; Roberts and Lean, 2008). Thus, our focus is on the effect that one area of precipitation has on another area of precipitation farther downstream.

2.2. *Non-advective PV tendency and piecewise PV inversion*

The local non-advective change in PV with time is calculated in order to examine the extent to which lower tropospheric PV anomalies are diabatically generated or enhanced (as performed in Raymond (1992), Cammas *et al.* (1994), Lackmann (2002), and Brennan and Lackmann (2005)), where P is Ertel's potential vorticity and $\mathbf{V}_\mathrm{h}$ is the horizontal wind vector:

$$P = g\,(f\mathbf{k} + \nabla_3 \times \mathbf{V}_\mathrm{h}) \cdot \nabla_3\theta \tag{1}$$

and $\mathbf{Y}$ is the non-advective PV flux vector

$$\mathbf{Y} = -\frac{\mathrm{d}\theta}{\mathrm{d}t}(f\mathbf{k} + \nabla_3 \times \mathbf{V}_\mathrm{h}) + \nabla_3\theta \times \mathbf{F} \tag{2}$$

with ∇_p being the quasi-horizontal gradient operator on an isobaric surface, ∇_3 the three-dimensional gradient operator $\left\{\nabla_p - \mathbf{k}\left(\frac{\partial}{\partial p}\right)\right\}$, and $\mathbf{F}$ the frictional force vector. Horizontal and vertical advections of PV were computed for the PV anomalies discussed in each case. Values of these terms were small in comparison to $\mathbf{Y}$, indicating that the PV was generated *in situ* and not advected in from elsewhere. Idealized simulations have shown that boundary layer friction can baroclinically generate positive PV anomalies that are advected out of the boundary layer via the warm conveyor belt (Adamson *et al.*, 2006; Plant and Belcher, 2007). The effect of moist dynamics on this mechanism has yet to be fully investigated with a simulation involving real data, and would therefore be well suited for an independent investigation. Thus, in the interest of focusing

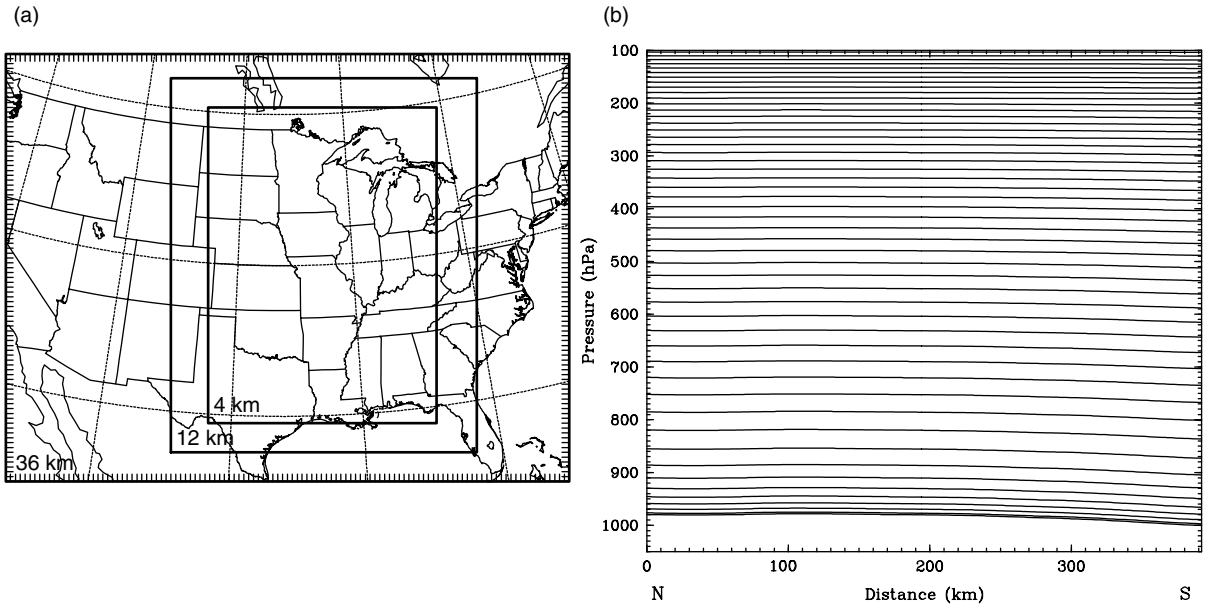

Figure 1. (a) WRF model domain locations with grid spacing indicated in lower left. (b) Cross-section of model vertical levels.

on the role of diabatic processes alone, the effect of friction on the PV structure will not be considered here, despite its potential contribution to the PV shown. Diabatic heating is directly output from the WRF (the sum of heating from the microphysics, convective, radiation and planetary boundary layer parametrization schemes).

To quantify the impact of various PV anomalies, piecewise PV inversion is conducted on both WRF and NARR data, using the methodology outlined by Davis and Emanuel (1991) in which the nonlinearity in the inversion is retained. The nonlinear balance equation provides the balance condition for the inversion (Charney, 1955). In order to ensure numerical convergence to a solution, the piecewise inversion is conducted on the entire 36 km (outermost) grid of the WRF. Piecewise PV inversion requires the specification of an appropriate reference state to quantitatively define the anomalies, thus filtering out the planetary-scale flow. We use the climatological mean flow for the time in question, in the form of the NARR mean computed over 1979–2001 for the appropriate month. Comparison with inversions performed with the more traditional time mean approach yielded similar results. Seventeen levels are used in the inversion, ranging from 950 to 150 hPa, with an interval of 50 hPa. Potential temperatures at 925 hPa and 175 hPa are used for the lower and upper boundary conditions, respectively. Lateral boundary conditions are set to zero, as the area of interest remains far from the lateral boundaries. To avoid inversion of PV (or potential temperature) at grid points below ground in the western USA, PV is set equal to zero for underground points. The 925 hPa level has been chosen as the lower boundary, as this level is above the model-parametrized planetary boundary layer heights throughout the non-elevated portions of terrain (the majority of the domain).

In each case, the atmosphere was partitioned into four parts:

(1) upper-level perturbation PV: all negative perturbation PV (θ) and positive perturbation PV (θ) with RH $<$70% from 500 hPa through to 175 hPa boundary θ;
(2) lower boundary: all positive and negative perturbation θ at 925 hPa;
(3) moist interior PV: all positive perturbation PV with RH $\geqslant$70% from 900 hPa to 400 hPa (inclusive);
(4) remaining interior PV: all negative perturbation PV and positive perturbation PV with RH $<$70% from 900 hPa through to 550 hPa.

The sum of the partitioned layers adds up to the total perturbation PV (with no PV inverted twice), as no moist positive perturbation PV exists above 400 hPa in either case. The partitioning separates tropopause-level PV, which descends no lower than 500 hPa in these events, from PV not of stratospheric origin, which exists up to 400 hPa. While this method of partitioning does not guarantee that all of the perturbation PV in partition 3 was due to diabatic processes, the calculation of the non-advective PV generation rates suggest that diabatic processes were involved in generating PV near the areas of precipitation. The PV anomalies in partition 4 are likely remnants of diabatically generated PV, sometimes referred to as 'cloud-wake' PV that is left behind as gradients in diabatic heating continue to generate PV farther downstream (Reed *et al.*, 1992). As will be discussed, the PV in partitions 2 and 4 is associated with smaller magnitudes of low- to mid-level balanced deformation in the WRF and the NARR. Thus, PV anomalies in partition 3, which were more recently generated by diabatic heating, will be the focus of our analysis. Individual PV anomalies from within partition 3 were selected for inversion where appropriate.

The perturbation wind field resulting from the inversion of selected PV has been used to calculate derived fields, including piecewise deformation and piecewise moisture flux, the latter of which was first presented in Lackmann *et al.* (1998). The same approach can be used to calculate piecewise frontogenesis, using the perturbation flow as input to the Petterssen (1936) two-dimensional (2D) frontogenesis equation. This approach was first quantitatively applied in Morgan (1999), and further demonstrated in Korner and Martin (2000). As presented in Morgan (1999), the 2D balanced frontogenesis function, F, may be separated into n

components ($k = 1, \ldots, n$) attributable to the PV partitions 1–4 previously discussed, plus those due to the mean PV and the irrotational part of the flow:

$$F^k = \frac{1}{|\nabla\theta|}\left\{-\left(\frac{\partial\theta}{\partial x}\right)^2\frac{\partial}{\partial x}u'_k - \frac{\partial\theta}{\partial y}\frac{\partial\theta}{\partial x}\frac{\partial}{\partial x}v'_k - \frac{\partial\theta}{\partial x}\frac{\partial\theta}{\partial y}\frac{\partial}{\partial y}u'_k - \left(\frac{\partial\theta}{\partial y}\right)^2\frac{\partial}{\partial y}v'_k\right\}. \quad (3)$$

The full thermal gradient is used, rather than the thermal gradient associated with each PV partition. While the components of frontogenesis are linear in the velocity fields, nonlinearity exists in the temperature field, making the inclusion of the temperature perturbations intractable. The piecewise frontogenesis presented here will not include the effects of convergence, as the flow recovered through the piecewise PV inversion techniques used here only included the non-divergent component of the wind. It is possible to use more advanced inversion techniques to recover the balanced divergent (irrotational) circulation (e.g. Davis *et al.*, 1996; Wang and Zhang, 2003), but the additional complexity was not deemed necessary to illustrate the relation between PV anomalies and frontogenesis in these cases.

3. 13–15 February 2003

3.1. Event overview

Over the 12 h period spanning 14/12 UTC through to 15/00 UTC, a surface cyclone develops in the lee of the Rocky Mountains and deepens to less than 1000 hPa as it moves eastward (Figure 2(b) and (d)). The surface cyclone's movement is associated with a tropopause undulation advancing from the southwest, implying positive PV advection above the surface low, as is commonly observed during cyclogenesis (e.g. Hirschberg and Fritsch, 1991). The undulation descends to below 350 hPa at its lowest point at 14/12 UTC (Figure 2(b)). The output from the WRF simulation (Figure 2(a) and (c)) depicts a slightly weaker surface cyclone which remains above 1000 hPa along the same track as the cyclone in the NARR. The simulated tropopause undulation in the WRF descends below 400 hPa at 15/00 UTC (Figure 2(c)).

Differences in precipitation are illustrated through the comparison of WRF 4 km composite simulated reflectivity (Stoelinga, 2006) (Figure 3(a)) and observed composite reflectivity (Figure 3(b)) at 14/06 UTC. At 14/06 UTC, the WRF inaccurately simulates convection (circled in Figure 3(a) and (b)) along a warm front (seen as a pressure trough extending east of the surface low in Figure 2). This convection is to the west of a northwest–southeast oriented rain band that is appropriately simulated. As previously discussed, further investigation of the reasons for these discrepancies is beyond the scope of this article. By 14/09 UTC, the northern edge of the convective region becomes more sharply defined in the WRF, with weaker reflectivities located farther north (circled in Figure 3(c)). The observations do not show a strong reflectivity gradient in the same location, and precipitation is more widespread in this area (circled in Figure 3(d)). Through the period 14/12 UTC–14/18 UTC, the WRF fails to accurately simulate the strengthening and increase in areal coverage of this secondary area of precipitation (circled in Figure 3(e) for the WRF and Figure 3(f) for the NARR). Comparison of precipitation over the span of the event (13/18 UTC–15/18 UTC) indicates that the WRF underestimates precipitation amounts by 10 to 30 mm in the circled area (not shown).

The difference in the development of this secondary area of precipitation by the WRF and NARR is most evident from 14/12 UTC onward. At 14/12 UTC, the NARR depicts strong 700 hPa frontogenesis in the vicinity of where stratiform precipitation had developed prior to 14/12 UTC (Figure 3(b) and (d)), and a secondary area of weak frontogenesis near the developing precipitation to the northwest (circled in Figure 4(b)). While the WRF, like the NARR, has frontogenesis associated with the stratiform precipitation at 14/12 UTC, it shows a secondary area of frontogenesis (circled in Figure 4(a)) developing to the west. In both the WRF and NARR, the least stable air (assessed using saturated equivalent potential vorticity, SEPV: Schultz and Schumacher, 1999) is located to the southwest of the secondary areas of frontogenesis.

To further investigate the reasons for the maintenance (or dissipation) of precipitation located downstream of the primary area of precipitation (circled in Figure 3(c) and (d)), cross-sections at 14/12 UTC are taken along a line extending northeastward from the least stable air through the secondary areas of frontogenesis (as indicated on Figure 4(a) and (b)). The secondary frontogenesis in the WRF is in the southwest portion of the cross-section, associated with the least stable air (Figure 5(a)). The secondary frontogenesis in the NARR is farther northeast (Figure 5(b)), with the WRF exhibiting weaker frontogenesis in this same area. In contrast with the WRF, the unstable air extends farther to the northeast in the NARR, and the air mass is saturated with respect to ice. In summary, at 14/12 UTC, the NARR features instability, frontogenesis and saturated conditions in the area where secondary precipitation developed (circled in Figure 3(f)), while the WRF is more stable, had weaker frontogenesis, and is unsaturated in the same area.

The most striking difference between the WRF and NARR is in the instability field, which was similar along the cross-section at 14/09 UTC (not shown). The 3 h time tendency (ending at 14/12 UTC) of potential stability in the 600–700 hPa layer, along with the 600 hPa vertical motion at 14/12 UTC, are presented to further investigate why the instability in the WRF is confined to the south (Figure 5(c) and (d)). Positive values (dark shading) of stability tendency indicate that $(-\partial\theta_e/\partial p)$ is becoming more stable with time, while negative values (light shading) indicate destabilization. The air is destabilizing along the cross-section in the NARR (Figure 5(d)). In the northeast part of the cross-section, upward motion is present in the NARR, corresponding with the moisture, frontogenesis and instability seen in this region (Figure 5(b)). An area of stabilization is present in the WRF (circled in Figure 5(c)) in an area of downward motion at 600 hPa. Ascent is present at 700 hPa (not shown), which increases the stability in the layer. In addition, the horizontal advection of instability implied by the 650 hPa winds in the WRF (Figure 4(a)) is weaker than in the NARR (Figure 4(b)). Calculation of the static stability tendency equation (Bluestein, 1993, pp 376–379) confirms that compression of the air column in the vertical and differential θ_e advection contribute to a net increase in potential stability in the WRF. The environment in the WRF prevents the development of secondary precipitation that was observed over the next 6 h in the NARR (Figure 3(f)),

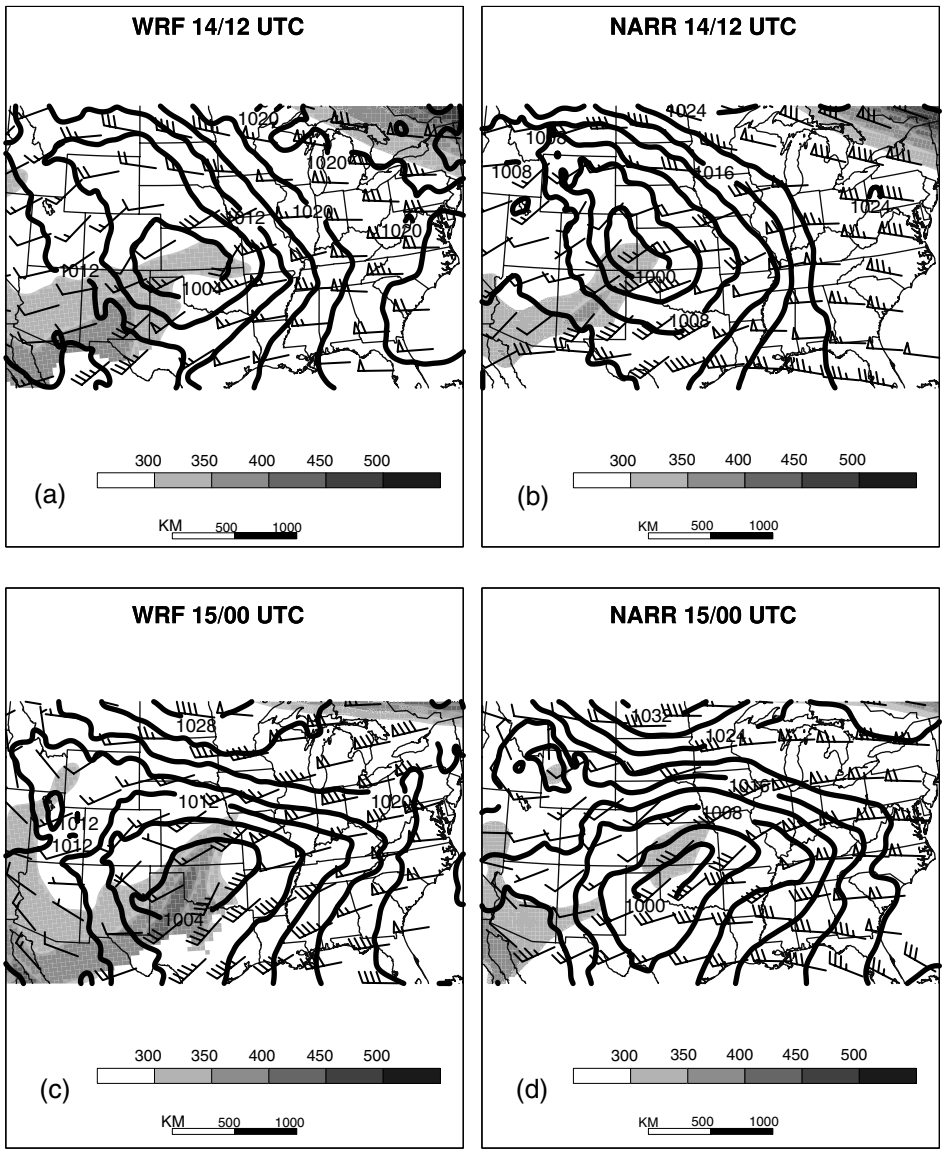

Figure 2. Pressure (shaded; hPa) and winds (barbs; m s^{-1}) on the 1.5 PVU surface, sea-level pressure (contours; 4 hPa interval) from WRF at (a) 1200 UTC 14 February 2003, (c) 0000 UTC 15 February 2003, and (b), (d) NARR for same respective times.

which continued through to 15/00 UTC (not shown). Accordingly, a diabatically generated PV anomaly is not observed in the WRF, as will be shown in section 3.2.

The secondary area of frontogenesis in the NARR strengthens as the precipitation intensifies (Figure 3(f)) through to 14/18 UTC (circled in Figure 4(d)). During the same time period, the stability increases slightly to the southwest of the strengthening frontogenesis (Figure 4(b) and (d)). By 14/18 UTC, the WRF depicts an axis of frontogenesis which is farther south than the NARR (circled in Figure 4(c)). As less stable air is located on the warm side of the frontogenesis in the WRF, this implies that the frontal circulation is farther south in the WRF versus the NARR. A new band of precipitation forms in the WRF between 14/18 and 15/00 UTC on the warm side of the frontogenesis (not shown). In summary, moisture is available for the initiation of banded precipitation in both the NARR and the WRF in the presence of weak stability. The primary difference is in the placement and strength of the axis of mid-level frontogenesis which provides the lift to realize this instability.

3.2. *PV analysis*

The discrepancy in the location of the 700 hPa frontogenesis is due to differences in the mid-level wind and temperature fields. At 14/06 UTC, the WRF simulates 700 hPa perturbation PV as high as 0.75 to 1 potential vorticity units (PVU) (Figure 6(a)). In contrast, the NARR depicts negligible values of perturbation PV in the same area (not shown). Note that the perturbation PV in the WRF is collocated with the strongest convection shown in the 4 km simulated reflectivity (Figure 3(a)). A cross-section through the mid-level PV anomalies in the WRF indicates that diabatic heating exceeds 7 K h^{-1} in a deep layer from 450 to 650 hPa (Figure 6(b)). The non-advective PV tendency reaches 8 PVU (3 h)$^{-1}$ directly beneath the maximum in diabatic heating in a layer from 550 to 700 hPa. This is much larger than the values of horizontal and vertical PV advection (not shown). Thus, there is sufficient evidence to suggest that most of the mid-level PV present at 700 hPa in the WRF was generated via diabatic heating, and has not been advected into the region from elsewhere.

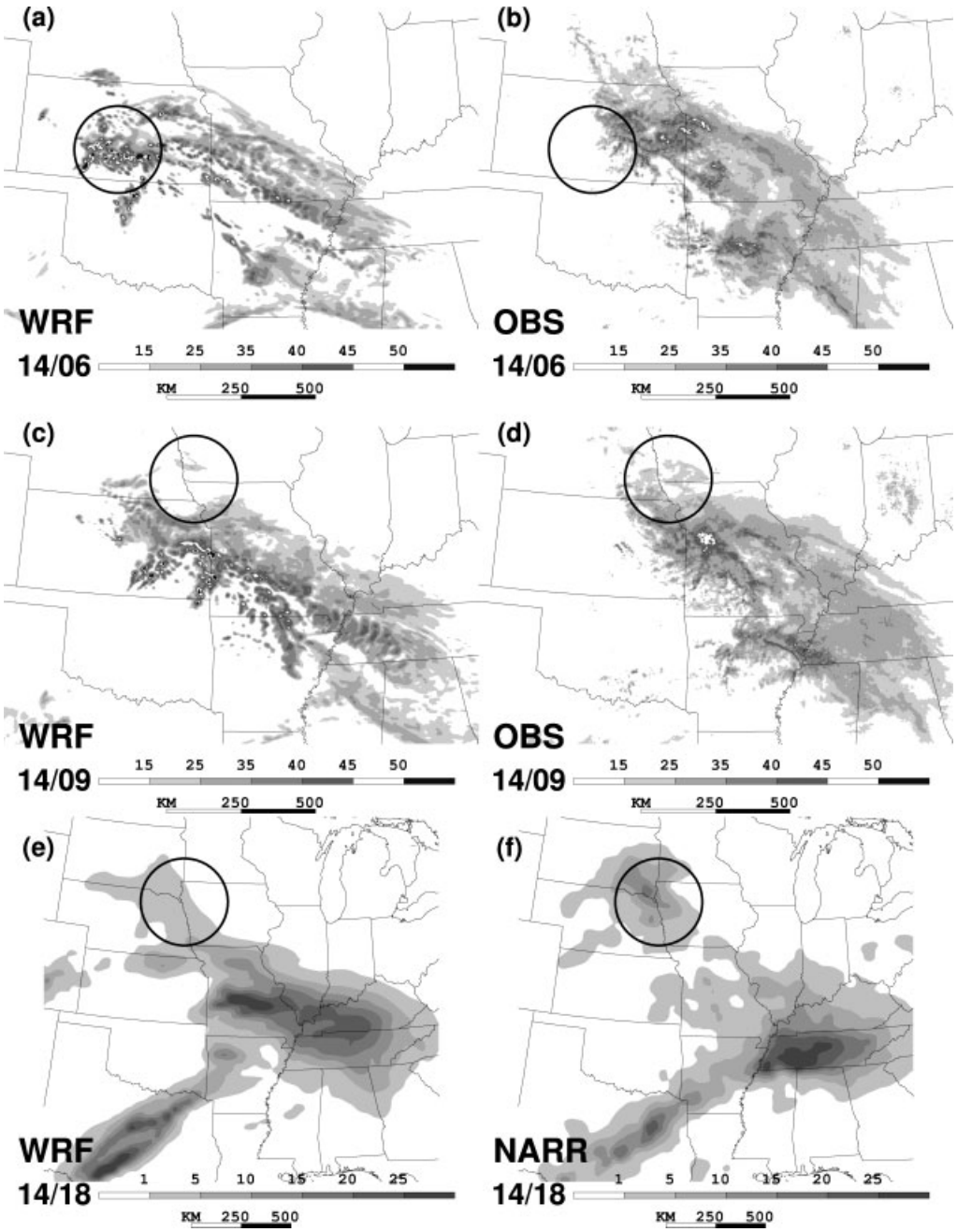

Figure 3. WRF composite simulated reflectivity (shaded; dBZ) at (a) 0600 UTC 14 February 2003 and (c) 0900 UTC 14 February 2003 (b), (d) WSR-88D Level III composite reflectivity (shaded; dBZ) for same times. Previous 6 h accumulated precipitation (mm) from WRF ending at (e) 1800 UTC 14 February 2003, and (f) NARR for same respective times.

By 14/12 UTC, the 700 hPa perturbation PV in the WRF has reached values greater than 1 PVU along a northwest–southeast oriented line (labelled PVA in Figure 7(a)). The NARR does feature PV in the same region, but it is smaller in coverage and magnitude, maximizing at 0.5 to 0.75 PVU (labelled PVA in Figure 7(b)). Note that both the WRF and NARR 700 hPa perturbation PV fields correspond quite well with the locations of precipitation maxima at 14/09 UTC (Figure 3(c) and (d)). By 14/18 UTC, PVA in the WRF has expanded northeast, with values of 0.75–1.0 PVU in the western portion of PVA and greater than 1.0 PVU in the eastern portion (Figure 7(c)). In contrast, the PVA anomaly is farther east in the NARR, with a weaker magnitude of 0.5 PVU (Figure 7(d)). Also, by 14/18 UTC, the location and orientation of the 700 hPa perturbation PVA is similar to that of the 700 hPa frontogenesis seen in both the NARR (Figure 4(d)) and WRF (Figure 4(c)). A secondary maximum in perturbation PV in the NARR at 14/18 UTC (labelled PVB in Figure 7(d)) is associated with precipitation that formed and was maintained in this area beginning at 14/12 UTC (see Figure 3(f)), as previously discussed. A secondary maximum located farther west in the WRF (labelled PVB in Figure 7(c)) is associated with weaker precipitation that began after 14/12 UTC, which then moved to the west. As this area of diabatically generated PV moved westward, it merged with low-level PV which was advected away from the elevated terrain in the Rocky Mountains (not shown).

Piecewise inversion of the upper-level PV anomalies (partition 1) demonstrates that the tropopause undulation

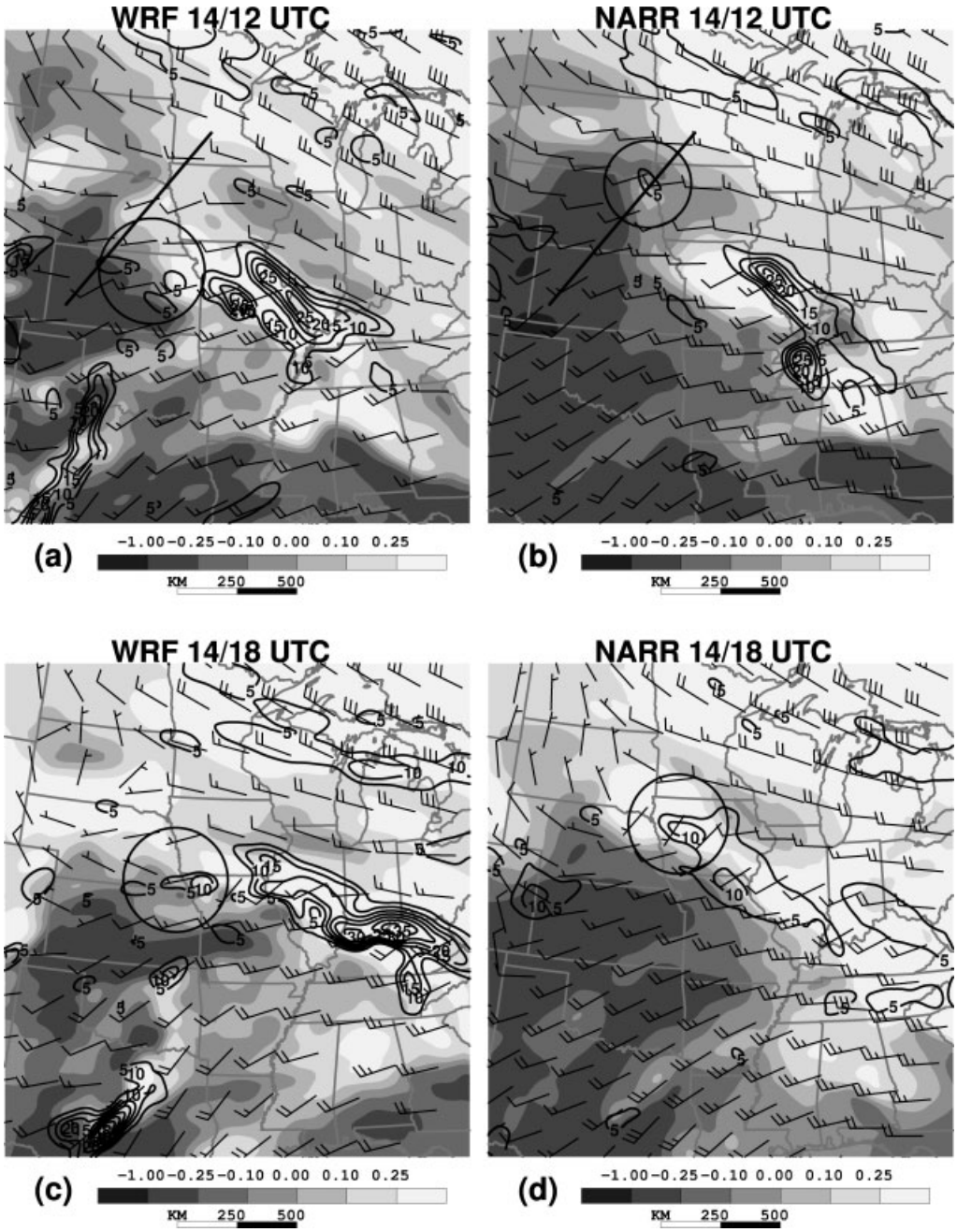

Figure 4. 700 hPa Petterssen frontogenesis (contours; 5 K (100 km)$^{-1}$ (3 h)$^{-1}$), 700–600 hPa average saturated equivalent potential vorticity (shaded; PVU), and 650 hPa winds (barbs; m s^{-1}) from WRF at (a) 1200 UTC 14 February 2003, (c) 1800 UTC 14 February 2003, and (b), (d) NARR for same respective times.

had a similar effect on the 700 hPa heights and flow in the NARR and WRF at both 14/12 and 14/18 UTC, and therefore will not be shown. Notable differences between the WRF and the NARR are evident in the height and winds at 700 hPa associated with the low- to mid-tropospheric PV in moist air (partition 3; Figure 8). At 14/12 UTC, the trough in the perturbation flow that extends southeast of the maximum negative height perturbation is oriented from northwest to southeast in the NARR (Figure 8(b)), in contrast to its more west to east orientation in the WRF (Figure 8(a)). The maximum in balanced deformation resulting from the perturbation wind field marks the location of the trough, which rotates cyclonically over the period. By 14/18 UTC, the balanced deformation in both the NARR (Figure 8(d)) and WRF (Figure 8(c)) is coincident with the location of the 700 hPa frontogenesis shown in Figure 4(d) and (c), respectively. Therefore, the low- to mid- tropospheric PV anomalies are associated with a wind field that influenced where the 700 hPa frontogenesis would develop.

While the temperature perturbations associated with the inverted PV anomalies cannot tractably be used as input into the balanced frontogenesis equation, examining their structure can still be instructive when paired with the perturbation deformation. Thus, the hypsometric equation was solved to find the temperature perturbation in the 650 to 750 hPa layer, using the perturbation heights from the inversion as input. The resulting perturbation temperature gradients at 14/18 UTC are shown for the WRF (Figure 9(a)) and the NARR (Figure 9(b)). The magnitude of the perturbation temperature gradient is larger in the WRF, and

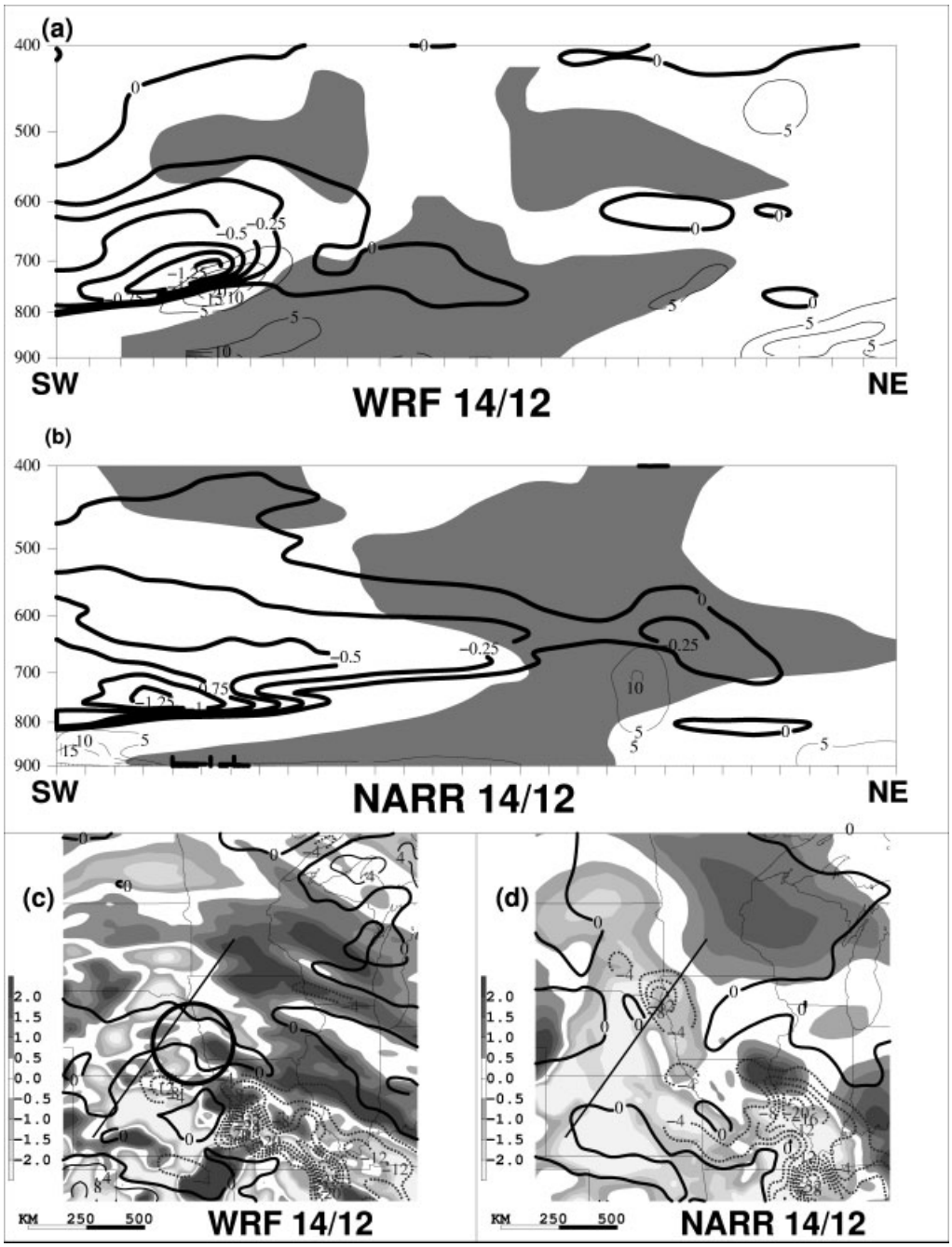

Figure 5. Cross-section of Petterssen frontogenesis (thin contours; 5 K (100 km)$^{-1}$ (3 h)$^{-1}$), saturated equivalent potential vorticity (thick contours; 0.25 PVU, only negative values shown), and relative humidity with respect to ice (shaded; >95%) from (a) WRF and (b) NARR at 1200 UTC 14 February 2003. Location of cross-section shown in Figure 4(a) and (b), and Figure 5(c) and (d). 3 h tendency of potential stability over the 600–700 hPa layer ending at 1200 UTC 14 February (shaded; K (100 hPa)$^{-1}$ (3 h)$^{-1}$; negative values indicate increasing instability) and 600 hPa vertical motion (contours; 0.4 Pa s^{-1}) from (c) WRF and (d) NARR at 1200 UTC 14 February.

is collocated with the axis of balanced deformation shown in Figure 8(c). The relation between the perturbed temperature gradient in the NARR and the axis of balanced deformation in Figure 8(d) is more tenuous. In both the WRF and the NARR, the piecewise frontogenesis (Figure 9(a) and (b), respectively) is in a similar location as the full frontogenesis (Figure 4(c) and (d), respectively). This analysis suggests that the temperature gradient and wind fields associated with the low- to mid-tropospheric PV anomalies affect the location of the maximum frontogenesis in both the NARR and the WRF.

In both the NARR and WRF, the low- to mid-tropospheric PV in moist air (partition 3) accounts for 60% of the total balanced deformation in the region where the balanced deformation and the perturbation thermal gradient are collocated, with the remaining partitions accounting for 5 to 20% (not shown). In the interest of completeness, PVA and PVB (defined by the boxes in Figure 7(c) and (d)) at 14/18 UTC were inverted separately from each other and the results were compared. This analysis makes clear that the balanced deformation nearest to the minimum height perturbation in Figure 8(c) and (d) is primarily associated with PVB, while the balanced deformation along the trough east of the minima in perturbation heights is associated with PVA. This illustrates that, as expected, the magnitude of the

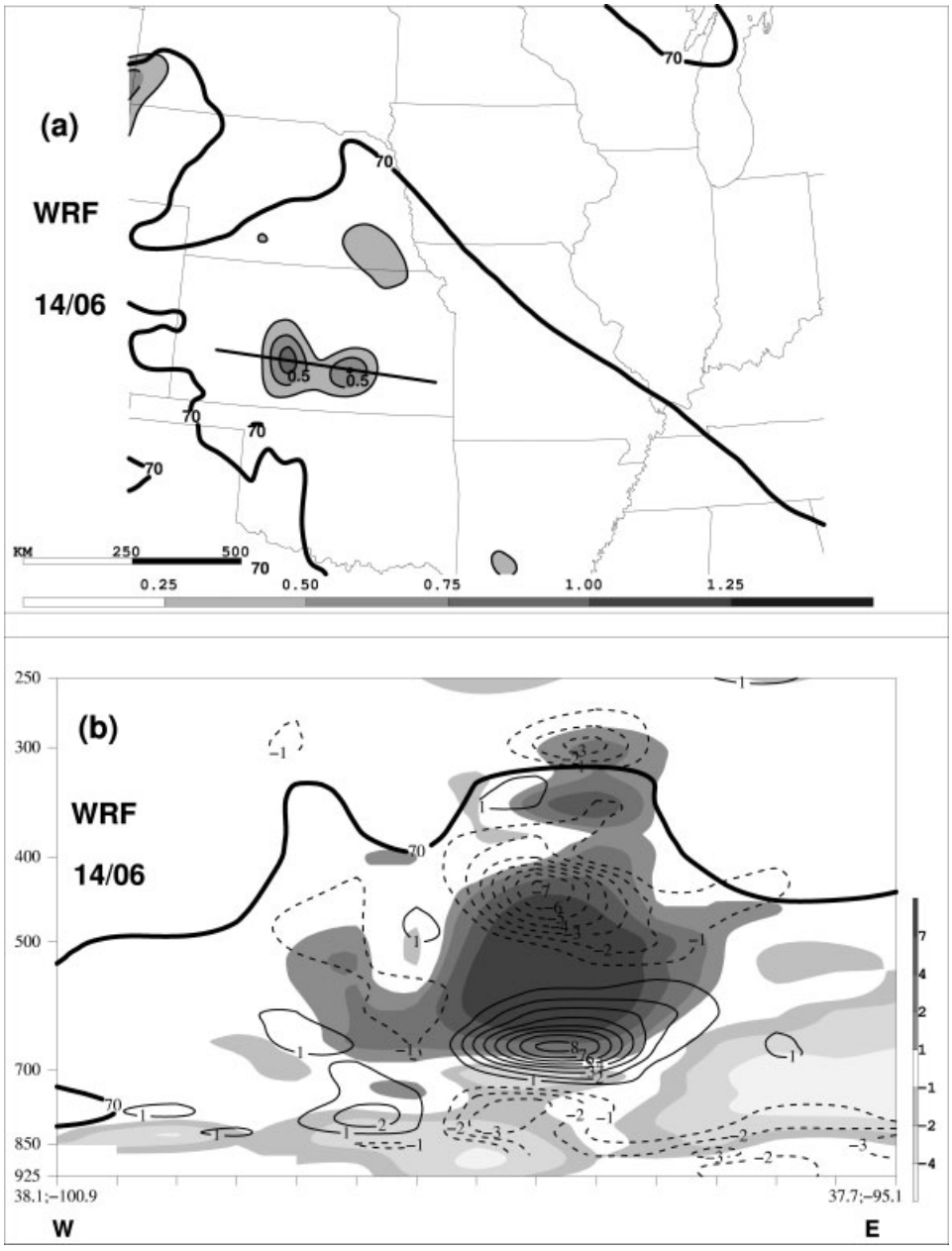

Figure 6. (a) 700 hPa PV (shaded; PVU) and 70% RH contour for 0600 UTC 14 February 2003 from WRF. (b) WRF cross-section as indicated in (a) of diabatic heating (shaded; 10^{-5} K s^{-1}), non-advective PV tendency (contours; 0.5 PVU (3 h)$^{-1}$), and 70% RH contour. All PV shown in (a) and all locations beneath the 70% contour in (b) are in moist air.

balanced deformation decreases with distance from the PV anomalies.

The WRF's incorrect rapid development of a diabatically generated PV anomaly (PVA in Figure 7(a) and (c)) is associated with the 700 hPa front developing along an east–west axis (circled in Figure 4(a) and (c)), farther south than in the NARR. The NARR depicts a northwest–southeast axis of frontogenesis (circled in Figure 4(b) and (d)), which is associated with a weaker PV anomaly generated via stratiform precipitation with embedded convection (PVB: Figure 7(b) and (d)). At 14/12 UTC, stabilization occurred in the WRF in the vicinity of PVB, preventing the development of a positive feedback between frontogenesis and diabatic PV generation that was seen in the NARR. The location of the 700 hPa front is a crucial factor in the underestimation of precipitation downstream of the convection in the WRF simulation, as this feature provides the lifting mechanism. It has been shown that the strength and placement of the PV anomalies are associated with both the temperature gradient and deformation fields, two key components of frontogenesis.

Finally, the relation between the low- to mid-level tropospheric PV anomalies and moisture flux downstream is examined. Figure 9(c) and (d) depict the 700 to 800 hPa average balanced moisture flux vectors resulting from the piecewise PV inversion. Areas circled represent the location of ongoing precipitation within the NARR data (Figure 3(f)), and solid lines indicate the axis of secondary frontogenesis (Figure 4(c) and (d)). At 14/18 UTC, the balanced moisture flux in the WRF (Figure 9(c)) in the northern part of the domain is directed well toward the north of the developing frontogenesis. To build on the inferences made from the balanced moisture flux, 24 12 h backward trajectories were initialised on the 4 km WRF grid from the area of

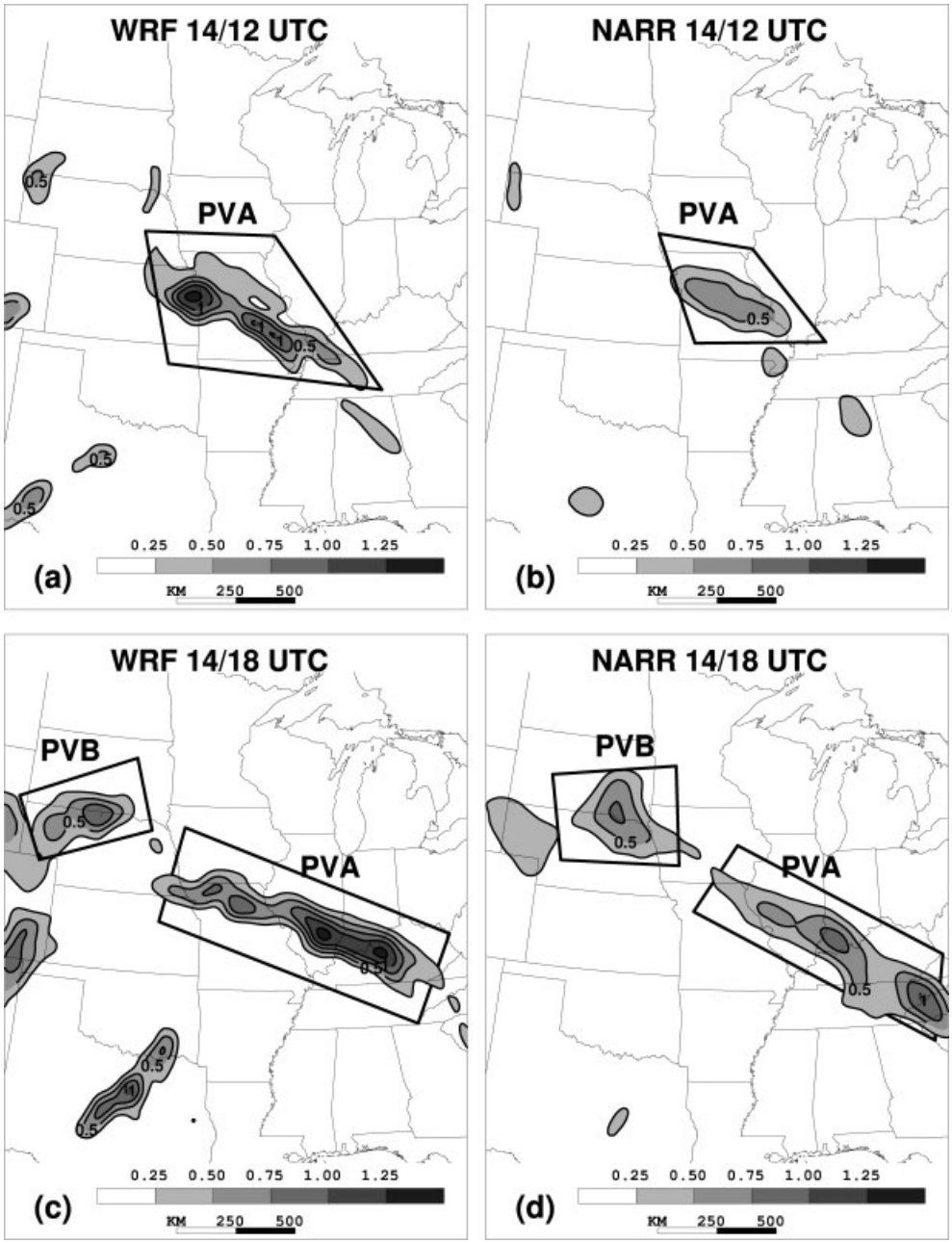

Figure 7. 700 hPa PV from partition 3 (shaded; PVU) for 1200 UTC 14 February 2003 from (a) WRF and (b) NARR, and for 1800 UTC 14 February from (c) WRF and (d) NARR.

precipitation (circled in Figure 3(e)) at 750 hPa. These trajectories depict warm conveyor belt air ascending across the warm front, with a loss of 1.6 g/kg (6.3 g/kg to 4.7 g/kg) of specific humidity, and relative humidities exceeding 90% along the latter half of the flow (values are averages over 24 trajectories). Thus, as air flows from the more intense precipitation toward the downstream precipitation, moisture decreases, but saturation is maintained. The balanced moisture flux in the NARR at the same time (Figure 9(d)) is slightly weaker, but is directed toward the developing frontogenesis. As balanced moisture transport exists toward roughly the same area in both the WRF and the NARR, yet only the NARR depicts notable precipitation in this area, it appears that the role of moisture flux was secondary to the location and orientation of frontogenesis associated with the PV anomalies.

4. 3–5 January 2005

4.1. Event overview

Over the 12 h period spanning 05/00 UTC through to 05/12 UTC, a surface cyclone develops in central Texas and deepens below 1012 hPa as it moves northeastward (Figure 10(b) and (d)). A southwest–northeast oriented thermal gradient develops north of the cyclone as a tropopause undulation approaches from the southwest. Through the 12 h period, the undulation descends to 450–500 hPa. The output from the WRF simulation is quite similar to the NARR, with the surface cyclone taking the same track and deepening at the same magnitude (Figure 10(a) and (c)). Two important differences include the 4 hPa stronger surface high to the north in the NARR throughout the simulation, and the more northeastward extension of the tropopause undulation

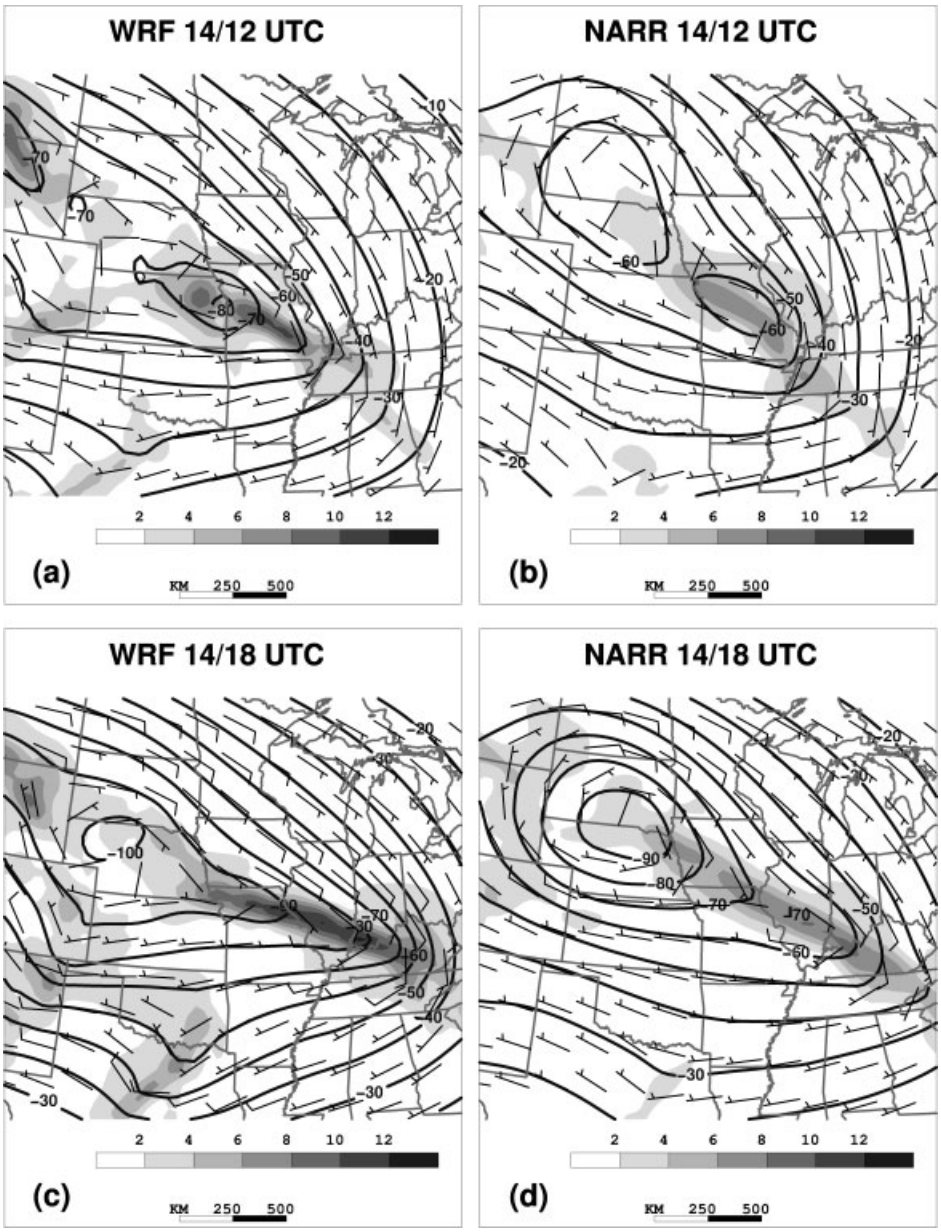

Figure 8. 700 hPa perturbation balanced heights (contours; 10 m), winds (barbs, m s^{-1}), and deformation (shaded; 10^{-5} s^{-1}) calculated using the inversion of PV from partition 3, for 1200 UTC 14 February 2003 from (a) WRF and (b) NARR, and for 1800 UTC 14 February from (c) WRF and (d) NARR.

into Nebraska and South Dakota at 05/12 UTC. Despite the relative similarity between the WRF and NARR with respect to the large-scale pattern, a notable difference in the distribution of precipitation between the two datasets is observed.

Through the period 05/06–05/12 UTC, both the WRF 4 km simulated reflectivity (Figure 11(a), (c) and (e)) and the observed composite reflectivity (Figure 11(b), (d) and (f)) depict rainfall throughout the Midwestern USA. Two differences exist: the WRF features reflectivities greater than 40 dBz throughout western Kansas (the evolution of this feature is circled in Figure 11), and is missing the widespread area of stratiform precipitation evident to its northeast. These differences are evident in the 12 h accumulated precipitation ending at 05/18 UTC (not shown). The primary difference scrutinized in this case lies in the WRF's excessive simulation of 5 to 15 mm of precipitation (in the form of snowfall) in the area circled in Figure 11(c) and (e), where the NARR indicates none to 5 mm fell.

Frontogenesis at 600 hPa is examined in this case, as frontogenesis at this level is best correlated with the location of this area of precipitation in the WRF. At 05/12 UTC, the NARR does not indicate 600 hPa frontogenesis (Figure 12(b)) in the area of precipitation circled in Figure 11(e) and (f), while the WRF depicts a southwest–northeast oriented region of frontogenesis in excess of 10 K $(100\ km)^{-1}$ $(3\ h)^{-1}$ (Figure 12(a)). The stability is lower in the NARR in this area, with values ranging from −0.25 to −1.0 PVU. The WRF is more stable to the southeast of the region of frontogenesis, with SEPV values of 0.0 to −0.1 PVU. SEPV was lower in the WRF three hours earlier at 05/09 UTC, indicating that some of the mid-level instability has likely been released in association with precipitation simulated in this area (Figure 11(c)). The WRF is saturated with respect to ice (relative humidity

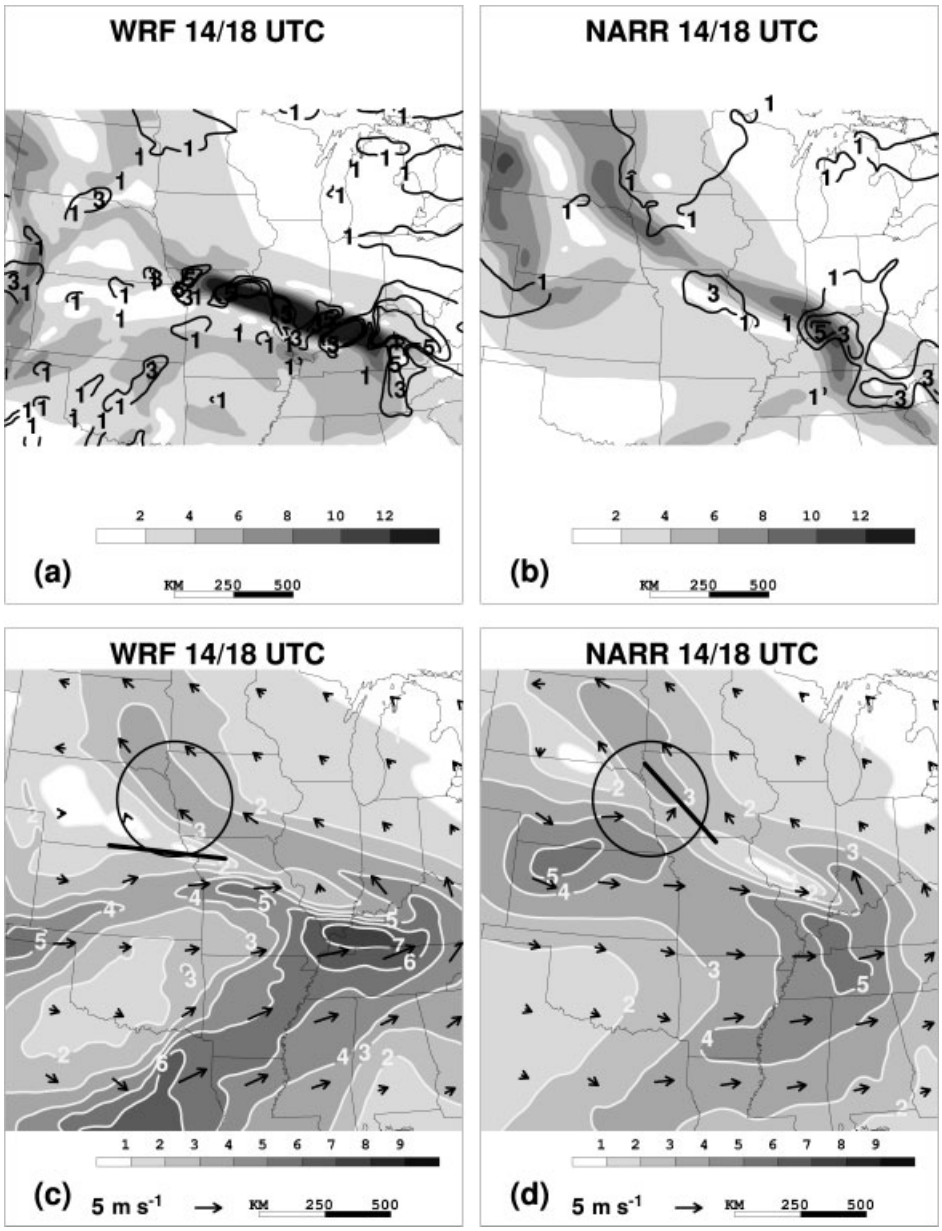

Figure 9. 700 hPa temperature gradient (shaded; °C (100 km)$^{-1}$) calculated using the inversion of PV from partition 3 and 700 hPa piecewise Petterssen frontogenesis calculated as described in text (contours; 1, 3, 5 K (100 km)$^{-1}$ (3 h)$^{-1}$), for 1800 UTC 14 February 2003 from (a) WRF and (b) NARR. 700–800 hPa average balanced moisture flux vectors and magnitudes (g kg^{-1} m s^{-1}) calculated using the inversion of PV from partition 3 for 1200 UTC 14 February from (a) WRF and (b) NARR, and for 1800 UTC 14 February from (c) WRF and (d) NARR. Solid line annotations represent approximate axis of frontogenesis as seen in Figure 4.

>95%) within the region of weaker stability, while the NARR is not saturated with respect to ice (relative humidity 85–90%; not shown). The frontogenetical circulation in the WRF, coupled with relatively small instability, is sufficient to generate precipitation. Although the NARR features greater instability, it lacks a mesoscale circulation and saturated conditions. This suggests that the real atmosphere is not able to realize the unstable environment.

4.2. *PV analysis*

As in the previous case, the mechanism for the development of low- to mid-tropospheric PV anomalies is investigated, and their associated height and flow fields are analysed. At 05/09 UTC, 600 hPa perturbation PV is examined (Figure 12(c)). The WRF depicts an east–west oriented line of perturbation PV (noted by a line indicating a cross-section shown in Figure 12(d)), while in the same area the PV in the NARR is negligible (not shown). Comparing the 600 hPa perturbation PV with the reflectivity fields (Figure 11(c) and (d)), the excess perturbation PV in the WRF is consistent with the greater amount of precipitation, and the lack of perturbation PV in the NARR with the relatively lower magnitude of precipitation. Note that the 600 hPa perturbation PV seen in the WRF is associated with the incorrectly simulated precipitation that was first observed in western Kansas at 05/06 UTC (Figure 11(a), circled), which has now moved farther east. A maximum in diabatic heating of 2–4 K h^{-1} is observed directly above an area of positive non-advective PV tendency in the 600–700 hPa layer ranging from 0.5 to 1.5 PVU (3 h)$^{-1}$ (Figure 12(d), western portion of cross-section). As in the previous case, the values of PV advection are much smaller

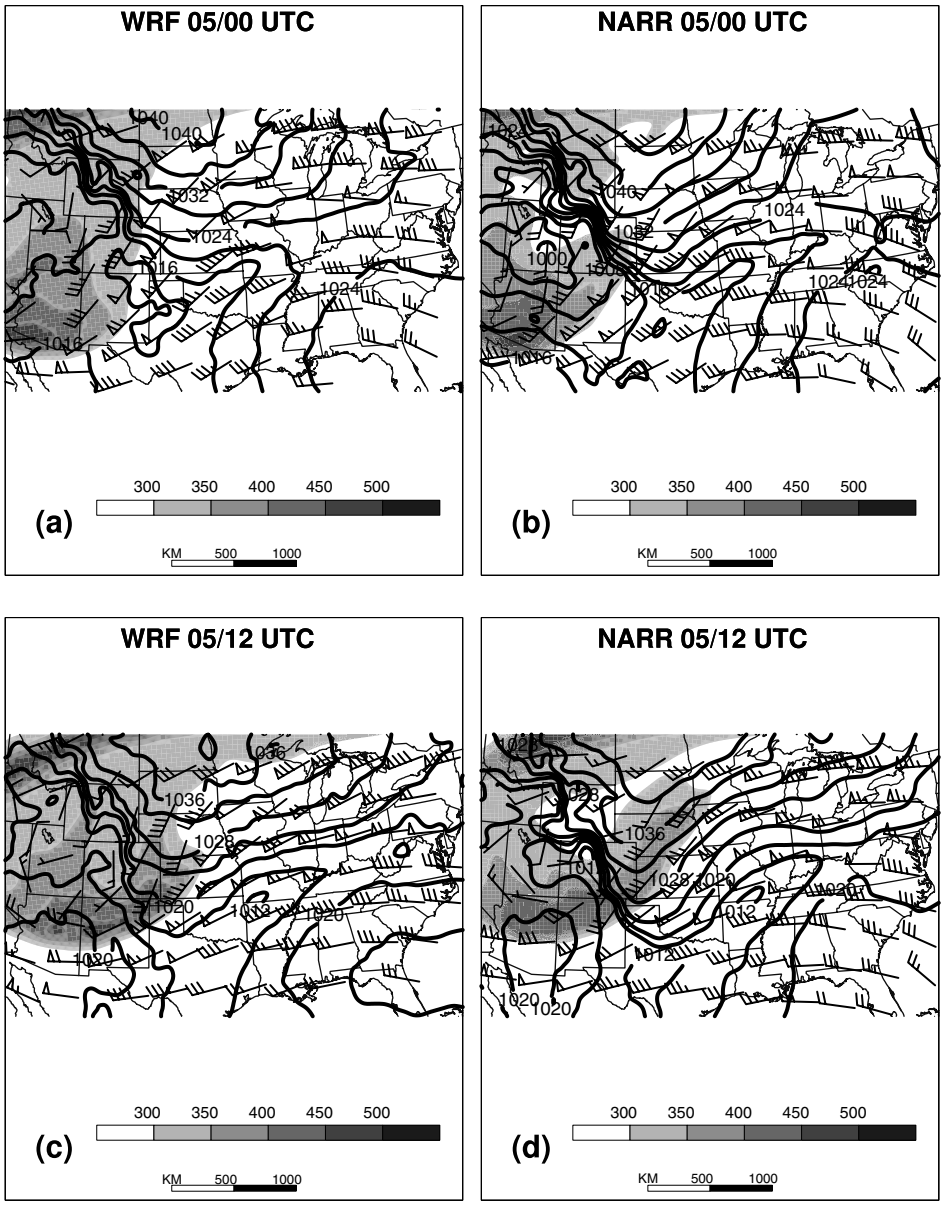

Figure 10. Pressure (shaded; hPa) and winds (barbs; m s^{-1}) on the 1.5 PVU surface, sea-level pressure (contours; 4 hPa interval) from WRF at (a) 0000 UTC 5 January 2005, (c) 1200 UTC 5 January, and (b), (d) NARR for same respective times.

than the non-advective PV tendency, which suggests that the perturbation PV in this region has been generated primarily by diabatic heating.

The low- to mid-level PV anomalies exhibit different magnitudes and spatial orientations with height, in contrast with the more vertically uniform anomalies seen in the previous case. Perturbation PV at 900 and 600 hPa is examined in Figure 13 for the WRF (left side) and the NARR (right side) for 3 h later, at 05/12 UTC. In both the WRF and NARR, the perturbation PV is higher in magnitude lower in the troposphere (labelled PVC), reaching 2.25 PVU at 900 hPa (Figure 13(a) and (b)) in the area of heaviest precipitation (seen for 05/12 UTC in Figure 11(e) and (f)). The perturbation PV at 900 hPa is similar in shape and magnitude in the WRF and the NARR. This low-level perturbation PV is distinct from that observed farther west in the WRF at 600 hPa (Figure 13(c), labelled PVD), which is not present in the NARR (Figure 13(d)).

As in the previous case, perturbation PV from partition 3 (low- to mid-tropospheric PV in moist air) is inverted, in this instance at 05/12 UTC. Piecewise inversion of the upper-level PV anomalies in partition 1 demonstrates that the tropopause undulation was associated with similar low- to mid-level height and flow perturbations in the NARR and WRF, and therefore will not be shown. At 600 hPa, the magnitude of the perturbation height anomaly is relatively similar between the WRF (Figure 14(a)) and NARR (Figure 14(b)). As in the February case, what differs is the strength and orientation of the balanced deformation (relevant areas boxed in Figure 14(a) and (b)). Note that the axis of 600 hPa balanced deformation in the NARR is largely collocated with the axis of 600 hPa frontogenesis seen in Figure 12(b), and the 600 hPa PV anomaly seen in Figure 13(d). The same is true for the WRF, with 600 hPa frontogenesis seen in Figure 12(a). In the WRF, the low- to mid-tropospheric PV in moist air accounts for 55% of the total balanced deformation in the region where deformation and the perturbation thermal gradient (Figure 14(e)) are collocated, with the remaining partitions accounting for 10 to 25%.

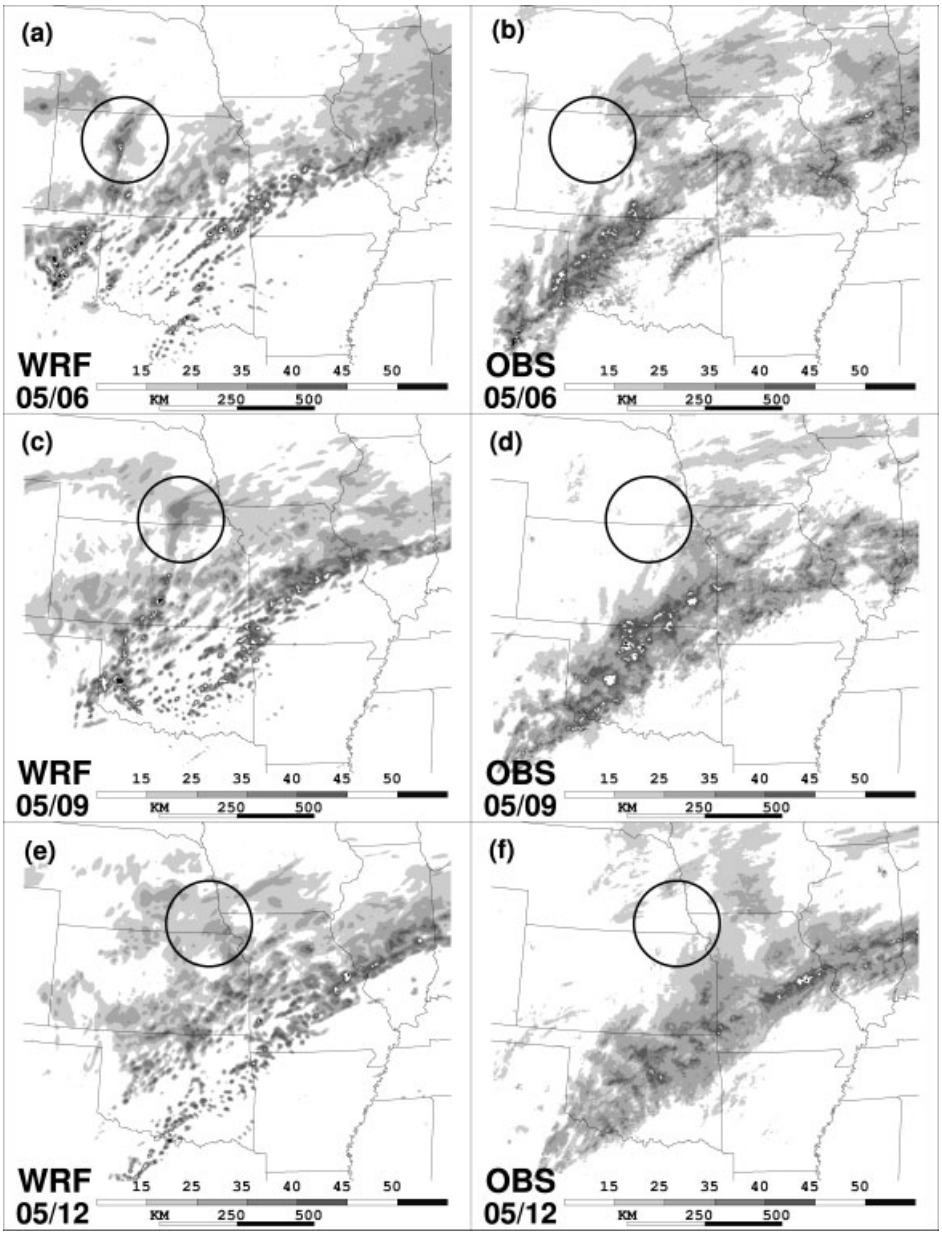

Figure 11. WRF composite simulated reflectivity (shaded; dBZ) at (a) 0600 UTC 5 January 2005, (c) 0900 UTC 5 January, (e) 1200 UTC 5 January (b), (d), (f) WSR-88D Level III composite reflectivity (shaded; dBZ) for same respective times.

As the perturbation PV was similar in the low levels (Figure 13(a) and (b)) and became increasingly different with height (Figure 13(c) and (d)), two more inversions were conducted to better clarify the relation between the varying PV and the flow field. The differences in PV with height first become apparent at 750 hPa, thus the PV in partition 3 was split into one partition below 750 hPa and one above (and including) 750 hPa. Results show that PV from 900 to 800 hPa is not associated with the 600 hPa balanced deformation (not shown). In the interest of completeness, the individual anomaly PVD in the WRF (defined by the box in Figure 13(c)) was inverted from 900 to 400 hPa. Approximately 75% of the balanced deformation boxed in Figure 14(a) is associated with this individual anomaly. This analysis confirms that it is in fact the PV anomaly in the WRF that extends above 750 hPa that is associated with the balanced deformation at 600 hPa.

The moisture flux from the balanced flow averaged over the 650 to 750 hPa layer also illustrates differences between the WRF (Figure 14(c)) and the NARR (Figure 14(d)). Higher-magnitude moisture flux is noted farther north in the WRF, with a ridge of stronger moisture flux directed northward (boxed in Figure 14(c)). This ridge is in part due to the fact that the WRF is 1 g kg^{-1} moister than the NARR in this area at 05/12 UTC (not shown). The difference in moisture flux also occurs due to the balanced flow associated with the perturbation PV at 600 hPa seen in Figure 13(c), where the NARR contains no perturbation PV (Figure 13(d)). To build on the inferences made from the balanced moisture flux, 24 21 h backward trajectories were initialised on the 4 km WRF grid from the area of precipitation (circled in Figure 11(e)) at 700 hPa. One-third of the trajectories originate in the warm air to the south, with the remaining two-thirds split evenly from the east and west. Averages taken over the eight trajectories that originate to the south depict a loss of 4.8 g/kg (8.6 g/kg to 3.8 g/kg) of specific humidity and relative humidities exceeding 94% along the flow. As in the previous case, as air flows from the

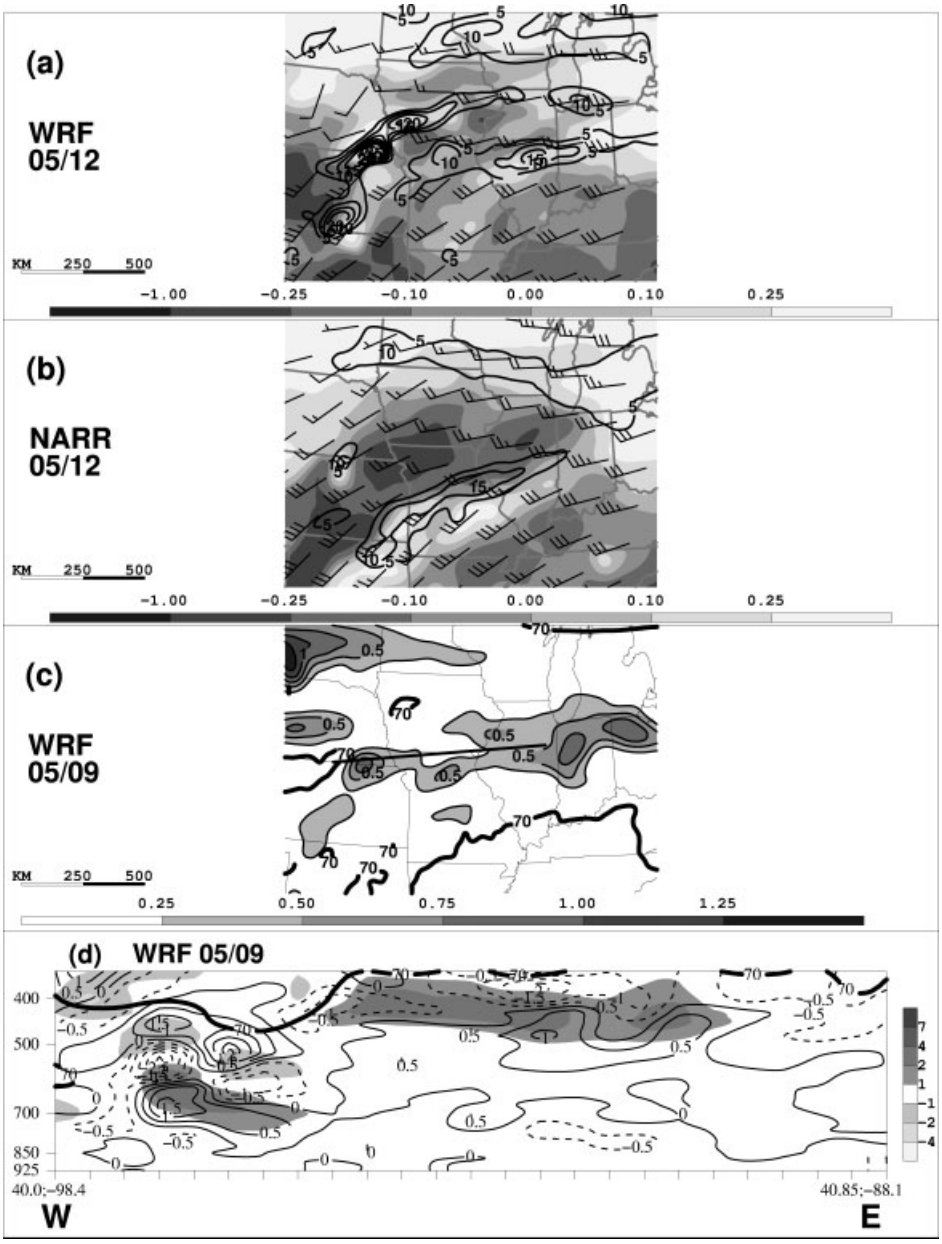

Figure 12. 600 hPa Petterssen frontogenesis (contours; 5 K (100 km)$^{-1}$ (3 h)$^{-1}$), 600–500 hPa average saturated equivalent potential vorticity (shaded; PVU), and 550 hPa winds (barbs; m s^{-1}) at 1200 UTC 5 January 2005 from (a) WRF and (b) NARR. 600 hPa PV (shaded; PVU) and 70% relative humidity contour for 0900 UTC 5 January from (c) WRF. (d) WRF cross-section as indicated in (c) of diabatic heating (shaded; 10^{-5} K s^{-1}), non-advective PV tendency (contours; 0.5 PVU (3 h)$^{-1}$), and 70% RH contour. All PV shown in (c) and all locations beneath the 70% contour in (d) are in moist air.

more intense precipitation to the downstream precipitation, moisture decreases, but saturation is maintained.

An analysis of the perturbation temperature gradients and piecewise frontogenesis is presented in Figure 14(e) and (f). The WRF (Figure 14(e)) simulates a larger magnitude gradient than the NARR (Figure 14(f)) due east of the maximum height perturbation (boxed in Figure 14(a)). This stronger temperature gradient is collocated with the larger-magnitude balanced deformation observed in the WRF (Figure 14(a)) versus the NARR (Figure 14(b)). The maximum piecewise frontogenesis is located in the aforementioned region (Figure 14(e)), and is in the vicinity of the maximum in frontogenesis from the full model output (Figure 12(a)). In contrast, the NARR contains no frontogenesis in this area, neither from the full model output (Figure 12(b)) nor the piecewise calculation (Figure 14(f)).

The perturbation PV generated by the most widespread convection, seen to the southeast of the snowfall, is simulated well by the WRF (PVC in Figure 13(a) and (b)). This PV is primarily in the lower troposphere, and is not directly related to the snowfall downstream, as confirmed by supplemental inversions. An area of incorrectly simulated precipitation farther west develops and moves northeastward over the period 05/06–05/12 UTC (circled in Figure 11). This results in PV production in the 600–700 hPa layer in the WRF (PVD in Figure 13), and an associated enhancement of the balanced deformation and northward balanced moisture flux (Figure 14(a) and (c)). This PV is shown to be associated with mid-tropospheric frontogenesis (Figure 14(e)). This frontogenesis enhances the lift of moist air streaming from the south associated with the primary area of convection, thus influencing the snowfall farther downstream. These

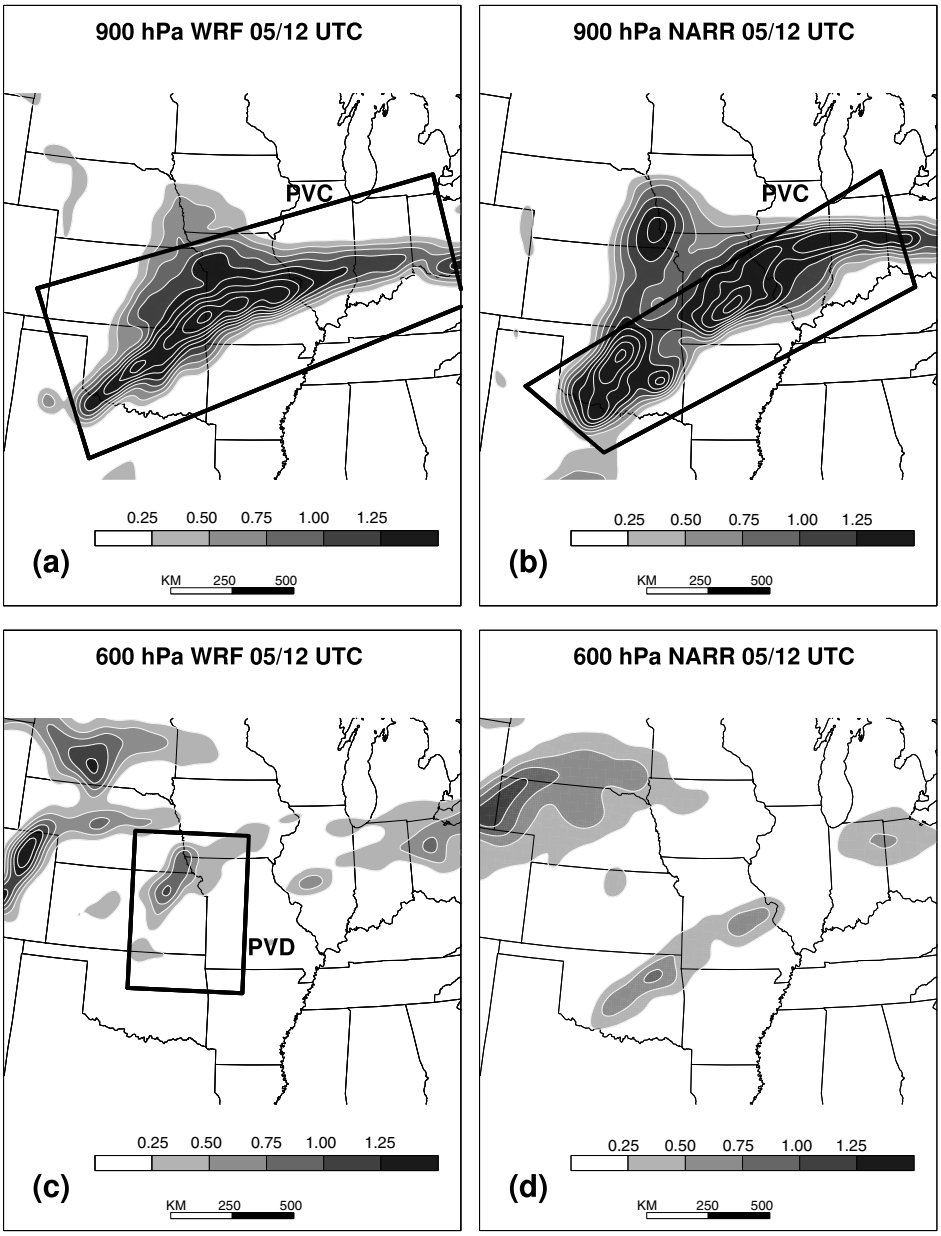

Figure 13. PV (shaded and contoured in white with an interval of 0.25; PVU) from partition 3 for 1200 UTC 5 January 2005 from WRF at (a) 900 hPa and (c) 600 hPa. (b), (d) PV from NARR for same time and same respective levels.

processes facilitate continued precipitation production in the area through to 05/18 UTC.

5. Summary of cases and discussion

Piecewise PV inversion was used to examine the role of low- to mid-tropospheric PV anomalies on the distribution of precipitation in two central USA winter storms. Output from WRF simulations were compared with NARR data, which served as a proxy for the observations. For the February case, 25 mm of precipitation was observed downstream from heavier precipitation, while the WRF simulated much lighter precipitation in the area. In the January case, 0 to 5 mm of precipitation fell downstream from heavier precipitation, while the WRF simulated 5 to 15 mm in this area. Note that any model that incorrectly simulates precipitation can result in an improper modification of mesoscale processes, which can impact downstream precipitation.

The inversion of the low- to mid-tropospheric PV anomalies in the February case made it evident that the location of the mid-level frontal band was associated with the distribution of the PV anomalies, which were primarily generated via diabatic heating. The inversion results demonstrate that the PV anomalies were not only associated with deformation within the frontal zone, but also with a thermal gradient in this region. By tracing back the origin of the PV anomalies, one could determine that the location of the frontal band would, in large part, be determined by whether convection developed over southern Kansas between 14/00 UTC and 14/06 UTC. While the particular orientation of the PV anomalies was associated with the orientation of the downstream moisture flux, moisture flux was of secondary importance to the frontogenesis associated with the PV anomalies, which provided the lifting mechanism.

The role of the low- to mid-tropospheric anomalies in the January case was more subtle and complex in

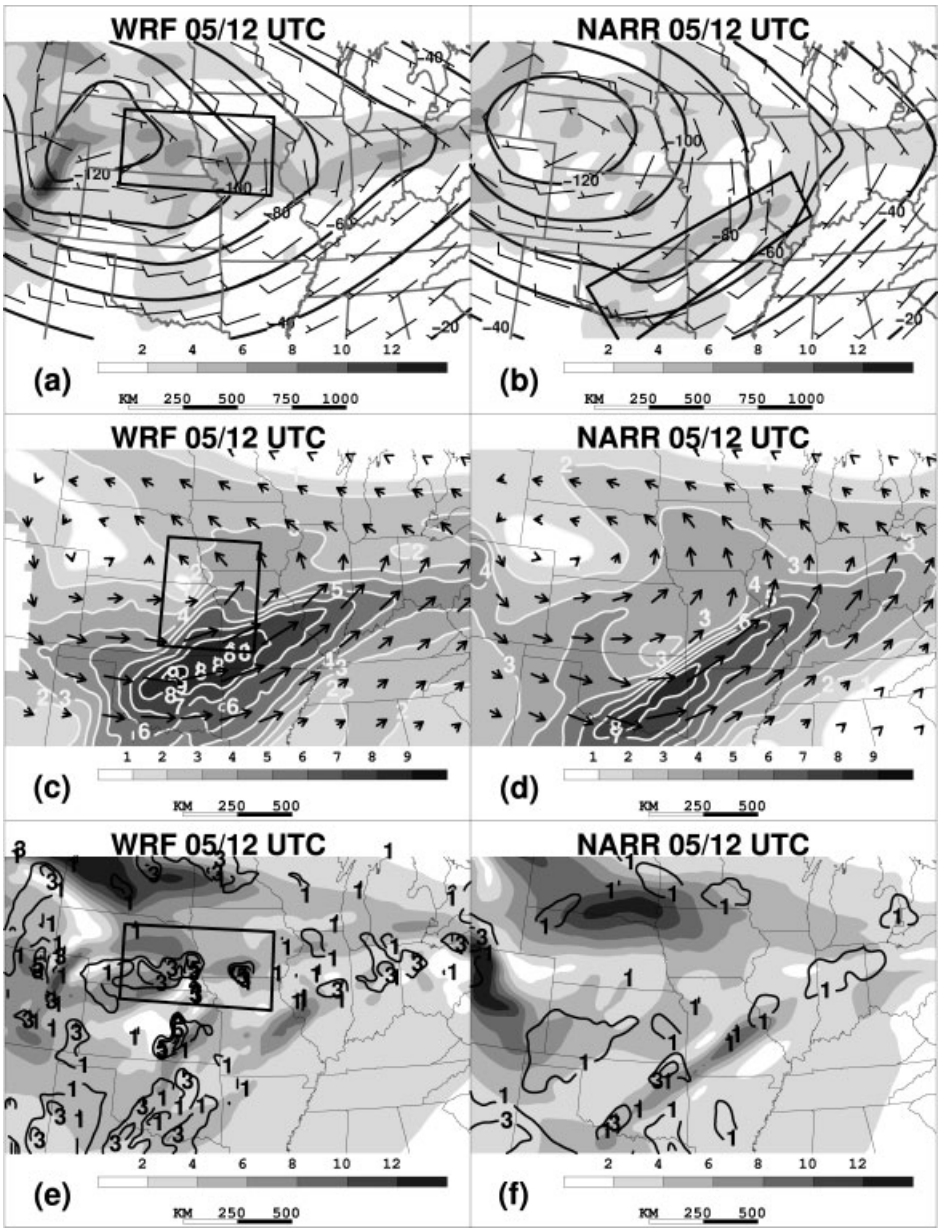

Figure 14. 600 hPa perturbation balanced heights (contours; 10 m), winds (barbs, m s^{-1}), and deformation (shaded; 10^{-5} s^{-1}) calculated using the inversion of PV from partition 3, for 1200 UTC 5 January 2005 from (a) WRF and (b) NARR. 650–750 hPa average balanced moisture flux vectors and magnitudes (g kg^{-1} m s^{-1}) calculated using the inversion of PV from partition 3 for 1200 UTC 5 January from (c) WRF and (d) NARR. 600 hPa temperature gradient (shaded; °C 100 km^{-1}) calculated using the inversion of PV from partition 3 and 600 hPa piecewise Petterssen frontogenesis calculated as described in text (contours; 1, 3, 5 K (100 km)$^{-1}$ (3 h)$^{-1}$), for 1200 UTC 5 January from (e) WRF and (f) NARR.

comparison to the February case. The WRF incorrectly simulated precipitation behind more east–west oriented convection located downstream. The diabatically generated PV associated with the east–west oriented convection was concentrated in the lower troposphere, and thus had minimal impact on the downstream precipitation, which was associated with mid-level frontogenesis. The frontogenesis aloft was associated with deformation produced by the PV anomalies associated with the incorrectly simulated precipitation, and led to enhanced lifting of moist air streaming northward from the convection to the south. Moisture flux in the mid-troposphere toward the area of incorrectly simulated snowfall was associated with the mid-tropospheric PV anomaly.

In both cases, the diabatically generated PV anomalies were associated with balanced deformation co-located with the perturbation temperature gradient. The piecewise frontogenesis generated by this configuration was in a similar location as the frontogenesis calculated by the full fields. It is probable that this results in a positive feedback process. As the enhanced frontogenetical circulation results in more diabatic heating, PV anomalies will strengthen and further enhance frontogenesis. This suggests that once a numerical model has improperly simulated strong diabatic heating, the model solution will further diverge from reality as the heating is reinforced by the developing frontogenesis. This occurrence opens the possibility that cases such as those presented here may suffer from reduced predictability.

6. Conclusions

Two cases were presented, one in which the WRF *underforecasts* downstream precipitation (February), and

another in which the WRF *overforecasts* downstream precipitation (January). These differences in precipitation were related to the strength of upstream PV anomalies. In the February case, the upstream PV in the WRF was of higher magnitude than in the NARR, and was associated with stronger than observed frontogenesis. This frontogenesis focuses lift and moisture away from the downstream region, resulting in an underforecast of downstream precipitation. In the January case, the upstream PV in the WRF is of lower magnitude and depth than seen in the NARR. The WRF also develops a PV anomaly downstream. This PV is associated with frontogenesis that focuses lift farther north, and a cyclonic circulation that transports moisture northward from the upstream precipitation. The frontogenesis and moisture transport thus result in an overforecast of downstream precipitation.

Based on the analysis of these cases, two general statements can be made which may be applicable to similarly structured events:

(1) Diabatically generated low- to mid-tropospheric PV anomalies are associated with flow and temperature perturbations that determine the location and magnitude of the mid-level front, or even its existence.
(2) These PV anomalies serve to enhance the flow of moisture northward on the eastern side of the anomalies, as they are associated with a cyclonic circulation.

As the latter point is well established, the importance of the former has been highlighted in this work. Both cases illustrate that the role of convection associated with warm fronts on downstream precipitation is more complex than simple 'robbing' of moisture. In events that feature widespread, long-duration convection, as both cases presented here did, the influence this convection has on downstream precipitation can be highly variable. The strength, depth and orientation of diabatically generated PV anomalies must be examined on a case-by-case basis to ascertain their specific influence on the environment. Thus, the cases analysed here do not provide a new conceptual model, or generalization which can be applied to any forthcoming event. Rather, they illustrate a methodology for analysing the role of convection in individual events.

Subsequent research could focus on further documenting the case-to-case variability of these types of events. The analysis performed here provides a framework that could be used to illustrate the relevant features and processes that are responsible for variability in precipitation forecasts amongst different model solutions. Thus, further research could investigate how weather forecasters can recognize when frontogenesis is being altered by diabatic processes within the model. Subsequent studies might also document how piecewise PV inversion could be used in similar events to improve quantitative precipitation forecasts, as PV inversions have been conducted within an operational setting at Météo-France (as described by Santurette and Georgiev (2005)) and the UK Met Office (Carroll and Hewson, 2005).

Acknowledgements

This research was supported by grant 207-62782 provided by the Cooperative Program for Operational Meteorology, Education, and Training. The views expressed herein are those of the authors and do not necessarily reflect the view of NOAA or its sub-agencies. The authors wish to thank Christopher Davis (NCAR) for his provision of the PV inversion code, Michael Brennan (TPC) for his modifications to this code, and Gary Lackmann (NC State) for his thoughtful review of an initial draft. The authors are grateful for the comments by two anonymous reviewers.

References

Adamson DS, Belcher SE, Hoskins BJ, Plant RS. 2006. Boundary-layer friction in midlatitude cyclones. *Q. J. R. Meteorol. Soc.* **132**: 101–124.
Banacos PC. 2003. 'Short-range prediction of banded precipitation associated with deformation and frontogenetic forcing.' Paper P1.7 in *Preprints, 10th Conference on Mesoscale Processes, Portland, Oregon.* Amer. Meteorol. Soc.
Baxter MA, Graves CE, Moore JT. 2005. A climatology of snow-to-liquid ratio for the contiguous United States. *Weather and Forecasting* **20**: 729–744.
Bluestein HB. 1993. *Synoptic-Dynamic Meteorology in Midlatitudes, Volume I Principles of Kinematics and Dynamics.* Oxford University Press.
Brennan MJ, Lackmann GM. 2005. The influence of incipient latent heat release on the precipitation distribution of the 24–25 January 2000 U.S. East Coast cyclone. *Mon. Weather Rev.* **133**: 1913–1937.
Cammas J-P, Keyser D, Lackmann GM, Molinari J. 1994. 'Diabatic redistribution of potential vorticity accompanying the development of an outflow jet within a strong extratropical cyclone.' Pp 403–409 in *Preprints, Int. Symposium on the Life Cycles of Extratropical Cyclones, Vol. II, Bergen.* Geophysical Institute, University of Bergen, Norway.
Carroll EB, Hewson TD. 2005. NWP grid editing at the Met Office. *Weather and Forecasting* **20**: 1021–1033.
Charney JG. 1955. The use of the primitive equations of motion in numerical prediction. *Tellus* **7**: 22–26.
Chen S-H, Sun W-Y. 2002. A one-dimensional time dependent cloud model. *J. Meteorol. Soc. Jpn* **80**: 99–118.
Davis CA, Emanuel KA. 1991. Potential vorticity diagnostics of cyclogenesis. *Mon. Weather Rev.* **119**: 1929–1953.
Davis CA, Grell ED, Shapiro MA. 1996. The balanced dynamical nature of a rapidly intensifying oceanic cyclone. *Mon. Weather Rev.* **124**: 3–26.
Dudhia J. 1989. Numerical study of convection observed during the Winter Monsoon Experiment using a mesoscale two-dimensional model. *J. Atmos. Sci.* **46**: 3077–3107.
Fowle MA, Roebber PJ. 2003. Short-range (0–48 h) numerical prediction of convective occurrence, mode, and location. *Weather and Forecasting* **18**: 782–794.
Fritsch JM, Murphy JD, Kain JS. 1994. Warm core vortex amplification over land. *J. Atmos. Sci.* **51**: 1780–1807.
Hertenstein RA, Schubert WH. 1991. Potential vorticity anomalies associated with squall lines. *Mon. Weather Rev.* **119**: 1663–1672.
Higgins RW, Shi W, Yarosh E, Joyce R. 2000. *Improved United States Precipitation Quality Control System and Analysis.* NCEP/Climate Prediction Center Atlas No. 7.
Hirschberg PA, Fritsch JM. 1991. Tropopause undulations and the development of extratropical cyclones. Part I: Overview and observations from a cyclone event. *Mon. Weather Rev.* **119**: 496–517.
Hong S-Y, Noh Y, Dudhia J. 2006. A new vertical diffusion package with an explicit treatment of entrainment processes. *Mon. Weather Rev.* **134**: 2318–2341.
Hoskins BJ, McIntyre ME, Robertson AW. 1985. On the use and significance of isentropic potential vorticity maps. *Q. J. R. Meteorol. Soc.* **111**: 877–946.
Jurewicz Sr ML, Evans MS. 2004. A comparison of two banded, heavy snowstorms with very different synoptic settings. *Weather and Forecasting* **19**: 1011–1028.
Kain JS. 2004. The Kain–Fritsch convective parameterization: An update. *J. Appl. Meteorol.* **43**: 170–181.
Kleinschmidt E. 1957. Cyclones and anticyclones. Pp 112–154 in *Dynamic Meteorology, Handbuch der Physik* **48**, Flugge S (ed.). Springer-Verlag.
Korner SO, Martin JE. 2000. Piecewise frontogenesis from a potential vorticity perspective: Methodology and a case study. *Mon. Weather Rev.* **128**: 1266–1288.
Lackmann GM. 2002. Cold-frontal potential vorticity maxima, the low-level jet, and moisture transport in extratropical cyclones. *Mon. Weather Rev.* **130**: 59–74.

Lackmann GM, Gyakum JR, Benoit R. 1998. Moisture transport diagnosis of a wintertime precipitation event in the Mackenzie River Basin. *Mon. Weather Rev.* **126**: 668–692.
Mahoney KM, Lackmann GM. 2007. The effect of upstream convection on downstream precipitation. *Weather and Forecasting* **22**: 255–277.
Mesinger F, DiMego G, Kalnay E, Mitchell K, Shafran PC, Ebisuzaki W, Jović D, Woollen J, Rogers E, Berbery EH, Ek MB, Fan Y, Grumbine R, Higgins W, Li H, Lin Y, Manikin G, Parrish D, Shi W. 2006. North American regional reanalysis. *Bull. Am. Meteorol. Soc.* **87**: 343–360.
Mlawer EJ, Taubman SJ, Brown PD, Iacono MJ, Clough SA. 1997. Radiative transfer for inhomogeneous atmospheres: RRTM, a validated correlated-k model for the longwave. *J. Geophys. Res.* **102**: 16663–16682.
Molinari J, Dudek M. 1992. Parameterization of convective precipitation in mesoscale numerical models: A critical review. *Mon. Weather Rev.* **120**: 326–344.
Moore JT, Graves CE, Ng S, Smith JL. 2005. A process-oriented methodology toward understanding the organization of an extensive mesoscale snowband: A diagnostic case study of 4–5 December 1999. *Weather and Forecasting* **20**: 35–50.
Moore RW, Montgomery MT, Davies HC. 2008. The integral role of a diabatic Rossby vortex in a heavy snowfall event. *Mon. Weather Rev.* **136**: 1878–1897.
Morgan MC. 1999. Using piecewise potential vorticity inversion to diagnose frontogenesis. Part 1: A partitioning of the Q vector applied to diagnosing surface frontogenesis and vertical motion. *Mon. Weather Rev.* **127**: 2796–2821.
Nicosia DJ, Grumm RH. 1999. Mesoscale band formation in three major northeastern United States snowstorms. *Weather and Forecasting* **14**: 346–368.
Novak DR, Bosart LF, Keyser D, Waldstreicher JS. 2004. An observational study of cold-season banded precipitation in northeast U.S. cyclones. *Weather and Forecasting* **19**: 993–1010.
Novak DR, Colle BA, McTaggart-Cowan R. 2009. The role of moist processes in the formation and evolution of mesoscale snowbands within the comma head of northeast U.S. cyclones. *Mon. Weather Rev.* **137**: 2662–2686.
Petterssen S. 1936. Contribution to the theory of frontogenesis. *Geofys. Publ.* **11**(6): 1–27.
Plant RS, Belcher SE. 2007. Numerical simulation of baroclinic waves with a parameterized boundary layer. *J. Atmos. Sci.* **64**: 4383–4399.
Posselt DJ, Martin JE. 2004. The effect of latent heat release on the evolution of a warm occluded thermal structure. *Mon. Weather Rev.* **132**: 578–599.
Raymond DJ. 1992. Nonlinear balance and potential-vorticity thinking at large Rossby number. *Q. J. R. Meteorol. Soc.* **118**: 987–1015.
Raymond DJ, Jiang H. 1990. A theory for long-lived mesoscale convective systems. *J. Atmos. Sci.* **47**: 3067–3077.
Reed RJ, Stoelinga MT, Kuo Y-H. 1992. A model-aided study of the origin and evolution of the anomalously high potential vorticity in the inner region of a rapidly deepening marine cyclone. *Mon. Weather Rev.* **120**: 893–913.
Ritchie EA, Holland GJ. 1997. Scale interactions during the formation of Typhoon Irving. *Mon. Weather Rev.* **125**: 1377–1396.
Roberts NM, Lean HW. 2008. Scale-selective verification of rainfall accumulations from high-resolution forecasts of convective events. *Mon. Weather Rev.* **136**: 78–97.
Rogers RF, Fritsch JM. 2001. Surface cyclogenesis from convectively driven amplification of midlevel mesoscale convective vortices. *Mon. Weather Rev.* **129**: 605–637.
Santurette P, Georgiev CG. 2005. *Weather Analysis and Forecasting: Applying satellite water vapor imagery and potential vorticity analysis*. Elsevier Academic Press.
Schultz DM, Schumacher PN. 1999. The use and misuse of conditional symmetric instability. *Mon. Weather Rev.* **127**: 2709–2732.
Schumacher PN. 2003. 'An example of forecasting mesoscale bands in an operational environment.' *Preprints, 10th Conference on Mesoscale Processes, Portland, Oregon.* Amer. Meteorol. Soc.
Shafran PC, Woollen J, Ebisuzaki W, Shi W, Fan Y, Grumbine RW, Fennessy M. 2004. 'Observational data used for assimilation in the NCEP North American Regional Reanalysis.' Paper 1.4 in *Preprints, 14th Conference on Applied Climatology, Seattle, Washington.* Amer. Meteorol. Soc.
Skamarock WC, Klemp JB, Dudhia J, Gill DO, Barker DM, Duda MG, Huang X-Y, Wang W, Powers JG. 2008. '*A description of the Advanced Research WRF Version 3*.' Available at: http://www.mmm.ucar.edu/wrf/users/docs/arw_v3.pdf.
Stoelinga MT. 1996. A potential vorticity-based study of the role of diabatic heating and friction in a numerically simulated baroclinic cyclone. *Mon. Weather Rev.* **124**: 849–874.
Stoelinga MT. 2006. '*A users' guide to RIP Version 4: A program for visualizing mesoscale model output*.' Available at: http://www.mmm.ucar.edu/mm5/documents/ripug_V4.html.
Wang X, Zhang D-L. 2003. Potential vorticity diagnosis of a simulated hurricane. Part I: Formulation and quasi-balanced flow. *J. Atmos. Sci.* **60**: 1593–1607.
Weisman ML, Skamarock WC, Klemp JB. 1997. The resolution dependence of explicitly modeled convective systems. *Mon. Weather Rev.* **125**: 527–548.
West GL, Steenburgh WJ, Cheng WYY. 2007. Spurious grid-scale precipitation in the North American Regional Reanalysis. *Mon. Weather Rev.* **135**: 2168–2184.
Zhang F, Snyder C, Rotunno R. 2003. Effects of moist convection on mesoscale predictability. *J. Atmos. Sci.* **60**: 1173–1185.
Zhang F, Bei N, Rotunno R, Snyder C, Epifanio CC. 2007. Mesoscale predictability of moist baroclinic waves: Convection-permitting experiments and multistage error growth dynamics. *J. Atmos. Sci.* **64**: 3579–3594.

